

## A CHANDRA SURVEY OF QUASAR JETS: FIRST RESULTS

H. L. MARSHALL<sup>1</sup>, D.A. SCHWARTZ<sup>2</sup>, J.E.J. LOVELL<sup>3</sup>, D.W. MURPHY<sup>4</sup>, D.M. WORRALL<sup>2,5</sup>, M. BIRKINSHAW<sup>2,5</sup>, J.M. GELBORD<sup>1</sup>,  
E.S. PERLMAN<sup>6</sup>, D.L. JAUNCEY<sup>3</sup>

*Submitted to Ap J Supplements, September 27, 2018, hlm*

### ABSTRACT

We present results from *Chandra* X-ray imaging and spectroscopy of a flux-limited sample of flat spectrum radio-emitting quasars with jet-like extended structure. Twelve of twenty quasar jets are detected in 5 ks ACIS-S exposures. The quasars without X-ray jets are not significantly different from those in the sample with detected jets except that the extended radio emission is generally fainter. New radio maps are combined with the X-ray images in order to elucidate the relation between radio and X-ray emission in spatially resolved structures. We find a variety of morphologies, including long straight jets and bends up to 90°. All X-ray jets are one-sided although the radio images used for source selection often show lobes opposite the X-ray jets. The FR II X-ray jets can all be interpreted as inverse Compton scattering of cosmic microwave background photons by electrons in large-scale relativistic jets although deeper observations are required to test this interpretation in detail. Applying this interpretation to the jets as a population, we find that the jets would be aligned to within 30° of the line of sight generally, assuming that the bulk Lorentz factor of the jets is 10.

*Subject headings:* galaxies:active — quasars

### 1. INTRODUCTION

Relativistic jets appear to be a common result of accretion in both stellar-mass and supermassive black hole systems. In an active galactic nucleus (AGN), a jet can transport energy from the sub-parsec scale central region to a distant hot spot and then to a radio lobe many times the size of the host galaxy. In many active galaxies, the radiative power of the jet is comparable to that of the nucleus and the kinetic energy flux can be comparable to the bolometric radiative luminosity of the core (Baum & Heckman 1989; Rawlings & Saunders 1991).

While jets are commonly detected in radio images of quasars and radio galaxies, jet detections in the X-ray band were rare before *Chandra*, being limited to the nearest and brightest active galaxies, principally Cen A, M 87, 3C 120, and 3C 273 and hotspots and jets in a few other objects. The sensitivity and high-quality imaging possible with *Chandra* now provides more detections (e.g. Schwartz et al. 2000; Worrall, Birkinshaw, & Hardcastle 2001; Sambruna et al. 2002, 2004). Many of the new discoveries are low power (FRI) radio sources, and BL Lac objects (Worrall, Birkinshaw, & Hardcastle 2001; Hardcastle, Birkinshaw, & Worrall 2001b; Pesce et al. 2002; Birkinshaw, Worrall, & Hardcastle 2001). In luminous quasars such as 3C 273 and PKS 0637-752, the jet physics is known to be different from that in low power sources, so it is important to increase the number of known X-ray jets in high power sources and, consequently, our knowledge of their range of properties. Two groups are addressing this need

through systematic surveys using *Chandra* observations of radio-selected quasars (Sambruna, et al.; this work).

Our survey was intended to discover whether radio jets commonly have X-ray emission that is as bright relative to their radio fluxes as in the brightest knot in PKS 0637-752 (Schwartz et al. 2000). For the sources with relatively bright jets, deep exposures would then provide more detailed measurements of individual jet components, as has been done, for example, for PKS 0637-752, 3C 273 (Marshall et al. 2001), M 87 (Marshall et al. 2002; Wilson & Yang 2002), and Cen A (Kraft et al. 2002; Hardcastle et al. 2003). In order to study particle acceleration and energy loss mechanisms in quasar jets, we need to assess key issues, such as whether the particle energy densities are in equipartition with the local magnetic field energy densities and whether the jets have high Lorentz factors in bulk motion oriented close to our line of sight Celotti et al. (2001); Tavecchio et al. (2000). In this paper, we describe the sample selection in section 2. In section 3, we describe the *Chandra* observations and compare the X-ray maps to newly obtained radio images. In section 4, we examine the sample properties in the context of beaming emission models. We use a cosmology in which  $H_o = 65 \text{ km s}^{-1} \text{ kpc}^{-1}$ ,  $\Omega_m = 0.3$ , and  $\Omega_\Lambda = 0.7$ .

### 2. SAMPLE SELECTION

We tailored our source selection criteria to generate a list of objects that have radio jets or nearby bright knots of suitable angular scale to resolve with *Chandra*. We selected targets from two complete samples for which radio maps were obtained with  $\sim 1''$  resolution at 1-10 GHz: a VLA sample of flat spectrum quasars ( $\alpha_r < 0.5$ , where  $S_\nu \propto \nu^{-\alpha}$ ) with core flux densities at 5 GHz ( $S_5$ )  $> 1 \text{ Jy}$  and  $\delta > 0^\circ$  (Murphy, Browne, and Perley 1993) and an Australia Telescope Compact Array (ATCA) survey of flat spectrum sources (Lovell 1997) from the Parkes catalog with core flux densities at 2.7 GHz greater than 0.34 Jy and  $\delta < -20^\circ$ . The portion of the sample derived from the ATCA survey is somewhat heterogeneous as not all sources are optically identified and two have redshifts less than 0.1; these low redshift sources are likely to be low luminosity FR I galaxies. Only sources

<sup>1</sup> Center for Space Research, Massachusetts Institute of Technology, 77 Massachusetts Ave., Cambridge, MA 02139, USA

<sup>2</sup> Harvard-Smithsonian Center for Astrophysics, 60 Garden St., Cambridge, MA 02138, USA

<sup>3</sup> CSIRO Australia Telescope National Facility, PO Box 76, Epping, NSW 2121, Australia

<sup>4</sup> Jet Propulsion Laboratory, 4800 Oak Grove Dr., Pasadena, CA 91109, USA

<sup>5</sup> Dept. of Physics, University of Bristol, Tyndall Ave., Bristol BS8 1TL, UK

<sup>6</sup> Joint Center for Astrophysics and Physics Department, Univ. of Maryland, Baltimore County, 1000 Hilltop Circle, Baltimore, MD, 21250, USA  
Electronic address: hermann@space.mit.edu

with emission that was found to be extended over scales  $> 2''$  were included as candidates. This selection takes advantage of the matched radio and X-ray telescope resolutions and of the excellent point spread function of Chandra:  $\lesssim 5\%$  of the core's power would be outside  $2''$ , so the X-ray intensity from the core at the location of the jet is expected to be negligible.

The extended radio flux densities were estimated for each object from previously existing radio maps of both samples and extrapolated to 5 GHz, if necessary. We then estimated the X-ray fluxes by assuming that the ratio of the 1 keV X-ray flux to the 4.8 GHz flux is the same as in the jet of PKS 0637–752, for which  $S_x = 25$  nJy and  $S_r = 0.7$  Jy. The predicted X-ray count rate is then about  $0.0010(S_x/\text{nJy}) \approx 0.0357(S_r/\text{Jy})$  count/s in the 0.5–7.0 keV band. We observed sources from the northern list where the predicted counts would be greater than 30 counts in 5 ks. For a region of interest that is about  $8'' \times 2.5''$ , the limiting count rates are much larger than the expected background of about 0.0001 count/s. The southern sample had more sources with bright extended flux, so the limit was set at 50 counts in 5 ks. These sources comprise our ‘‘A’’ list.

A ‘‘B’’ list was also generated from these two samples. The selection criterion was based entirely on the morphology of the extended emission from maps available before starting the survey: the radio emission was predominantly one-sided and linear. This criterion extends our sample to predicted count rate that are lower than expected for the targets in the A list. We include these sources in our list because we already know that radio surface brightness is not the only characteristic that sets the X-ray flux. Knot A1 of 3C 273, for example, has an  $S_x/S_r$  ratio that is  $10\times$  higher than for PKS 0637–752 (Marshall et al. 2001). The morphological selection criterion was efficient at picking out sources in the A list, so that many A-list targets would also qualify in the B list.

We note that both target lists are drawn from flux-limited samples based on radio flux without regard to redshift or optical properties. Our sample selection is somewhat different from that used by Sambruna et al. (2002, 2004) who selected sources from a list of known jets compiled from surveys of the literature. The completeness of the lists they used is not known. Six of their targets are also in our sample but of the remaining eleven, seven do not satisfy at least one of our sample requirements and four are in the declination gap ( $-20^\circ$  to  $0^\circ$ ) between the northern and southern surveys on which we have based our sample selection. By selecting our A targets on the basis of extended flux without regard to morphology, we pick up more highly bent and amorphous structures than are found in the lists used by Sambruna et al. Since any literature-based sample is biased to the northern hemisphere, it is not surprising that many of our new targets are in the southern hemisphere.

The full sample (Table 1) consists of 56 objects, comprised of 9 sources in the A list that are not in the B list, 21 sources that are in both lists, and 26 sources that are only in the B list. Of the 56 sources, 20 were observed as part of a *Chandra* observing program in cycle 3, and are the subject of this paper. A few sources in the sample have been observed in other observing programs and results will be included in a future paper where we will also include results from the continuing *Chandra* observing program.

### 3. OBSERVATIONS AND DATA REDUCTION

#### 3.1. Imaging results

The observation dates and exposure times for the 20 targets observed in *Chandra* observing cycle 3 are given in Table 2. Events in the 0.5–7.0 keV range were selected for all analysis and to form the X-ray images, shown in Fig. 1. The location of the X-ray core in each image was determined by computing a preliminary centroid by fitting Gaussians to the 1D histograms obtained from events within  $30''$  of the core. The final centroid was computed similarly using only events within  $3''$  of the preliminary centroid. The observed core count rate was estimated within a 2.5 pixel ( $1.23''$ ) radius aperture and the (negligible) background was taken from an annulus from 15 to  $20''$  from the core. For this size aperture and the typical quasar core spectra, the enclosed power is about 95% of the total power, so we did not apply an aperture correction to the observed count rates. Results are shown in table 4.

In all but one observation, ACIS was restricted to a 1/4 subarray with a field of  $2' \times 8'$  and a frametime,  $t_f$ , of 0.8 s. In one case, 0208-512, a 1/8 subarray (a  $2' \times 8'$  field of view) was used, for which  $t_f = 0.4$  s. For the brightest sources, pileup, which increases with frametime, may be a concern. Pileup diverts the grades of good events into bad grades, reducing the apparent count rate and shifting events to higher energies. The count rate reduction is greater than 10% when there are more than about 0.25 counts per frame, or at about 0.3 cps (0.6 cps) when  $t_f = 0.8$  s (0.4 s). There are three sources for which the *observed* core count rate exceeds the 10% loss count rate so that the reported count rate is systematically low by 10% or more: 1145–676, 1828+487, 2251+158. We computed independent estimates of the core count rates using the ACIS readout streak. The streak occurs as X-rays are received during the ACIS parallel frame transfer, which provides  $40 \mu\text{s}$  exposure in each pixel along the streak per frame. For an observation with a live time of  $T$  (yielding  $T/t_f$  frames), a section of the readout streak that is  $\theta_s$  arcsec long accumulates an exposure of  $t_s = 4 \times 10^{-5} T \theta_s / (t_f \theta_x)$  s, where  $\theta_x = 0.492''$  is the angular size of an ACIS pixel. For these observations,  $T \simeq 5$  ks and  $t_f = 0.8$  s (0.4 s), giving  $t_s = 7.6$  s (15.2 s) in a streak segment that is  $\theta_s = 15''$  long. For the three sources in question, the count rates estimated from the streak are systematically higher, as expected, although this is not significant for 1145-676 which appears to have a soft spectral excess (Table 4). While the count rate determined from the 2D image is more precise, it is subject to larger bias due to pileup. By contrast, the count rate determined from the streak is more uncertain but less biased; the streak-based count rates should be preferred for PKS 1145-676, 1828+487, and 2251+158. For 2251+158, pileup reduces the observed count rate by more than a factor of three.

New radio maps were obtained for many of the sources at the ATCA or the VLA. These will be reported in detail in a separate paper (Lovel, et al., in preparation). These new maps were used for the image overlays in Figure 1 (details of the radio contours are provided in Table 3), and were used to determine radio fluxes for the cores and jets. For the overlays, we assumed that the radio and X-ray cores coincided in order to register the X-ray and radio maps to better than  $0.1''$ . The applied shifts were  $\sim 1''$ .

We tested for the existence of an X-ray jet using simple test based on Poisson statistics. First, the radio images were used to define the position angles and lengths of possible X-ray jets. Most jets are clearly defined as one-sided structures but in a few ambiguous cases, the pc-scale jets were used to define the jet direction. The inner and outer radii,  $r_i$  and  $r_o$ , are given in Table 5 along with the position angle at which the

region was centered. The width of the rectangle was  $3''$  except for 1030-357, 1655-776 and 2101-490, where the jets bend substantially, so the rectangles were widened to  $10''$ ,  $10''$ , and  $5''$ , respectively. Profiles of the radio emission along the jets were extracted and are shown in fig. 2. In order to eliminate the wings of the core but avoid counterjets, a radio profile was determined at  $90^\circ$  to the jet and subtracted. Next, the X-ray counts in the same rectangular region defined by the radio data were compared to a similar sized region on the opposite side of the core for the test, assuming a Poisson probability distribution. We set the critical probability for detection of an X-ray jet to 0.0025, which yields a 5% chance that there might be one false detection in this set of 20 sources. Histograms of the X-ray emission along the jets are shown in Fig. 3. The jet and counter-jet position angles are compared, providing a qualitative view of the X-ray emission along the jets. In no case is a counter-jet apparent in the X-ray images. X-ray emission that is symmetrically distributed about a quasar core is ignored because it is either associated with the *Chandra* point response function (so it is more clear in bright sources such as 2251+158) or it could be an indication of hot gas in the potential well of a galaxy or small cluster of galaxies.

Jet X-ray fluxes (table 5) were computed from count rates using 1000 nJy per count/s. This conversion is accurate to about 10% for typical power law spectra. The spectral index from radio to X-ray is computed using  $\alpha_{rx} = \log(S_x/S_r)/\log(\nu_x/\nu_r)$ , where  $\nu_x = 2.42 \times 10^{17}$  Hz and  $\nu_r$  depends on the map used.

### 3.2. Core Spectral Fits

The X-ray spectrum of the nucleus of each source was measured using an extraction circle of radius 2.5 pixels (1.23 arcsec), with background measured from source-free regions from the same observation and the same CCD. Spectral fitting was performed in the energy band 0.5–7 keV; the low energy limit was set high enough to reduce any uncertainties in the ACIS contamination correction to an unimportant level. In each case the data were fitted with a power law with excess intrinsic absorption. The power-law slope,  $\Gamma_x$ , is the photon spectral index, and thus is  $\alpha_x + 1$ , where  $\alpha_x$  is the energy spectral index more commonly used in radio astronomy and in the inter-comparison of multiwavelength data. The X-ray results are given in Table 4.

The addition of a narrow  $K\alpha$  fluorescence line from neutral Fe at a (fixed) rest energy of 6.4 keV and (fitted) equivalent width 220 eV improved the fit significantly in only one quasar: 1202-262. The detection rate for this line is consistent with the findings by Gambill et al. (2003) using the Sambruna et al. sample, who find it in three of 16 quasars observed with *Chandra*, particularly given that their observations were of twice the duration of ours and their quasar X-ray cores are typically somewhat brighter than those we observed. Only two of our objects, 1828+487 and (particularly) 2251+158 showed the effects of pileup in the spectra, so for these sources we used the pile-up model in XSPEC (Davis 2001). Spectra of both these objects (the brightest of our sample) have been measured by earlier X-ray missions. Our result for the photon index of 1828+487 (3C 380) is in good agreement with the value of  $1.58 \pm 0.13$  ( $1\sigma$  uncertainty) found over 0.2–2 keV by Prieto (1996) with ROSAT. For 2251+158 (3C 454.3), our measurement is somewhat lower than the ROSAT results of  $1.62 \pm 0.04$  (Fossati et al. 1998) or  $1.73 \pm 0.1$  (Prieto 1996), but in good agreement with BeppoSax results of  $1.38_{-1.44}^{+1.26}$  (90% uncertainty) over

a more closely corresponding energy band (Tavecchio et al. 2002). A third object also observed previously, 0208-512, is reported from ASCA data to have a spectral index of  $1.66_{-0.09}^{+0.1}$  (Kubo et al. 1998) or  $1.69 \pm 0.04$  (Reeves & Turner 2000), and from BeppoSAX to have  $1.7_{-1.62}^{+1.96}$  (90% uncertainty, with an absorption feature at 0.6 keV of which there is no evidence in the *Chandra* data Tavecchio et al. 2002) in agreement with our value. Also observed with ROSAT in a pointed observation, it has a reported spectral index in the soft X-ray band of  $2.04 \pm 0.04$  (Fossati et al. 1998), suggesting either variability or a soft excess (see also Sambruna 1997). Soft excesses are not uncommon in quasar cores, and indeed the *Chandra* data suggest one is present in 1145-676 (Table 4).

Core radio and X-ray flux densities are plotted against each other in Fig. 4. The radio flux densities were measured from the maps shown in Fig. 1 and then adjusted to 5 GHz assuming  $\alpha_r = 0.25$ . The X-ray flux densities are estimated at 1 keV ( $2.42 \times 10^{17}$  Hz). The radio and X-ray maps were not obtained at the same time, so there will be additional scatter in Fig. 4 due to variability. The spectral indices between the radio and X-ray bands ( $\alpha_{rx}$ ) are centered on a value of 0.5 and the targets in subsample A are not distinguishable from those in subsample B, indicating that the morphology selection does not pick out targets with preferentially dim X-ray cores even though the extended radio fluxes are somewhat smaller. Similarly, jet detections are found without bias regarding either this spectral index or the radio or X-ray core flux densities.

The X-ray photon indices,  $\Gamma_x$ , are collected in Figure 5. We follow practice dating from the *Einstein* Observatory period of assuming that the underlying spectral-index distribution is Gaussian, and maximize the likelihood to find the best-fit underlying mean and dispersion, with 90% joint-confidence uncertainties, are  $\bar{\Gamma} = 1.59_{-0.09}^{+0.07}$  and  $\sigma = 0.13_{-0.05}^{+0.11}$ . The results are consistent with early X-ray measurements of the cores, and support the conclusion that flat-radio-spectrum quasars have flatter average X-ray spectra than radio-quiet quasars, consistent with a beamed radio-related component contributing to the X-ray emission from radio-loud quasars (see Worrall [1990] for a review). Gambill et al. (2003) found similar values of  $\bar{\Gamma} = 1.66$  and  $\sigma = 0.23$ , with our somewhat smaller value of  $\sigma$  possibly implying that our sample is more homogeneous in its selection. We find no obvious difference between our subsamples with and without jets.

### 3.3. Notes on Individual Sources

In this section, we present qualitative descriptions of the X-ray and radio morphologies shown in Figure 1 and describe the orientations of the polarizations or any pc-scale jets. Profiles of the radio and X-ray emission along the jets are given in figures 2 and 3, respectively.

#### 0208-512

Our ATCA image of 0208-512 shows a  $\sim 4''$  long jet at a position angle of  $-129^\circ$ , which is similar to the position angle of the milliarcsecond-scale radio jet (Tingay et al. 2002), indicating a straight jet from pc to kpc scales. X-ray emission is also seen in the arcsec-scale jet but fades drastically after a  $90^\circ$  bend in the radio jet (Fig. 1a). The radio polarization electric vectors in the  $4''$  jet are orthogonal to the jet direction but no polarized emission is detected in the jet after the bend. A more detailed analysis is presented by Schwartz et al. (2004).

#### 0229+131

The radio emission from 0229+131 shows a bright inner jet to the NE which bends to the east and weakens (Fig. 1b). There is also a weak westerly jet. VLBA images (e.g Fomalont et al. (2000)) show a milliarcsec jet which initially points to the NE but then bends to the east  $\sim 4$  mas from the core. We detect no associated extended X-ray emission.

#### 0413–210

The VLA image of 0413–210 reveals a two-sided radio jet. The brighter jet is to the SE for which there is a corresponding X-ray jet (Fig. 1c) and the radio polarization data show electric vectors orthogonal to the jet direction. This source has also been observed at milliarcsec resolution as part of the VLBA calibrator survey (Beasley et al. 2002) and shows a single-sided jet at a similar position angle to its arcsec-scale counterpart to the SE.

#### 0745+241

0745+241 shows a bright radio core with weak extended lobes. VLBA observations by Fomalont et al. (2000) show a one-sided jet to the NW indicating that the jet bends by  $\sim 40^\circ$  between the milliarcsec- and arcsec-scale structure. There are four photons (in a  $0.7''$  radius circle) associated with the western lobe at about  $7''$  from the core, which constitutes a detection at about the  $3.6\sigma$  level, where the background was determined in an annulus from  $6.0$  to  $8.8''$  (Fig. 1d). Otherwise, we detect no significant extended X-ray emission related to the radio emission.

#### 0858–771

Our ATCA image of 0858–771 shows a two-sided jet (Fig. 1e). No linearly polarized flux was detected in the core with a 3-sigma detection limit of 2 mJy. In the southern jet the electric vectors are orthogonal to the jet direction while in the northern jet the polarization structure is more complex. No polarized flux is detected along the weak inner part of the northern jet but the lobe is polarized by up to 12%. On the western side of the lobe, where the inner jet terminates, the electric vectors are parallel to the jet direction. However on the eastern side of the lobe the E-vectors have rotated by  $90^\circ$ . It is at the termination of the inner north jet where we find a few X-ray photons that do not comprise a significant detection of the jet or its termination. No VLBI data are available for this source to give an idea of the initial directions of the jets. We detect no associated extended X-ray emission.

#### 0903–573

The radio emission from 0903–573 reveals a one-sided arcsec-scale jet to the NE of the core and low-level extended emission (Fig. 1f). There is X-ray emission associated with the radio jet. The radio polarization E-vectors along the jet are at position angles between  $70^\circ$  and  $80^\circ$  compared to a jet direction of  $\sim 33^\circ$ . The milliarcsec-scale structure of this source is presently unknown.

#### 0920–397

There is a strong X-ray detection in the southern jet of 0920–397 (Fig. 1g). The X-ray brightness drops monotonically along the  $5''$  long inner jet and there is perhaps an X-ray detection coincident with the southern radio lobe (Fig. 1g). Data in the United States Naval Observatory Radio Reference Frame Image Database reveal a milliarcsec-scale jet to the

south indicating that the southern jet remains straight from pc to kpc scales. No radio polarization was detected in the jets of this object. A more detailed analysis is presented by Schwartz et al. (2004).

#### 1030–357

X-ray emission is marginally detected from the inner  $8''$  of the jet that has a slight bend towards the southeasterly of two bright radio features about  $13''$  from the core (Fig. 1h). Two X-ray bright, resolved knots are associated with the bright features, which may be interpreted as two  $90^\circ$  bends in the jet. The radio polarization electric field vectors are orthogonal to the jet direction at least as far as the first knot. New VLBI images show a jet about  $0.002''$  long at nearly the same position angle as the  $10''$  scale jet (Ojha 2004). A more detailed analysis of the X-ray and radio data is presented by Schwartz et al. (2004).

#### 1046–409

The radio structure of this source is somewhat confusing, with two knots to the northwest, a knot  $4''$  to the southeast at the beginning of an arc curving  $90^\circ$ , and amorphous emission  $20''$  in diameter centered on the core (Fig. 1i). X-ray emission is detected at the beginning of the arc to the southeast, which we interpret as the brightest part of a curved jet. Radio polarization E-vectors are orthogonal to the jet direction out to the first knot to the SE but are parallel to the jet direction at the end of the arc. VLBA observations by Fomalont et al. (2000) show a one-sided milliarcsec jet at a position angle similar to that of the initial direction of the southeast arcsec-scale jet. Once again the change in radio jet direction and polarization appears linked to the termination of the X-ray jet.

#### 1145–676

The one-sided jet curves slightly, ending in a resolved structure perpendicular to the jet (Fig. 1j). The western radio lobe is not symmetrically placed opposite the jet. X-ray emission is not formally detected from the jet when the entire jet length,  $40''$ , is used. Defining the selection region to be only  $5''$  long, however, does lead to the X-ray emission becoming significant. The radio polarization E-vectors are orthogonal to the direction of the inner  $5''$  jet.

#### 1202–262

This target has the brightest X-ray jet in our sample, with a  $\sim 30^\circ$  bend that follows the radio image until the radio jet takes a  $\sim 90^\circ$  bend (Fig. 1k). This jet is remarkable in that the flux in the jet is 10% of the power in the core (after accounting for pileup) while the highest jet/core ratio previously obtained was 7% for PKS 0637–752 (Schwartz et al. 2000). The radio data reveal polarization E-vectors perpendicular to the jet direction along the northern jet as far as the lobe  $6''$  from the core where the position angle has rotated by 90 degrees. On the milli-arcsecond scale there is also a jet aligned with the initial direction of the northern arcsec-scale jet (Fomalont et al. 2000). The southern radio lobe is well resolved and symmetrically positioned opposite the extended emission to the northeast. A more detailed analysis is presented by Schwartz et al. (2004).

#### 1258–321 = ESO 443–G024

The source has a low redshift ( $z=0.01704$ ) and extended radio morphology that is concentrated close to the core, indicating that this source is a low-power FR I radio source (Fig. 1l).

We do not detect X-ray emission associated with the radio jets. There may be X-ray emission from an extended halo of hot gas about  $10''$  across but we have not specifically tested this hypothesis.

#### 1343–601 = CEN B

This galaxy also has a low redshift ( $z = 0.01292$ ) but the radio morphology is clearly one-sided and shows a narrow jet with a few knots (Fig. 1m). A knot  $5''$  from the core is easily detected in the X-ray image as well as another region  $8''$  from the core. The polarized component of the radio emission shows E-vectors approximately perpendicular to the jet direction but shows some deviations, particularly at the brightest part of the X-ray jet. There is well-resolved X-ray emission of  $0.017 \pm 0.002$  count/s in a region spanning  $10\text{--}70''$  from the core, upstream of and coincident with the diffuse lobe. New VLBI images show a jet about  $0.020''$  long at nearly the same position angle as the  $10''$  scale jet (Ojha 2004).

#### 1424–418

1424–418 is one of the most compact radio sources in our sample. The radio data show a jet extending  $1''$  to the west of a compact core before becoming diffuse (Fig. 1n). We detect no associated extended X-ray emission.

#### 1655+077

This quasar ( $z = 0.621$ ) shows a compact radio core, a short jet extending to the SE and a jet extending  $2.5\text{--}3''$  to the NW before bending  $90^\circ$  to the SW (Fig. 1o). VLBA data show knots along a  $0.007''$  long jet to the NW (Fomalont et al. 2000). No X-ray emission was detected other than in the core.

#### 1655–776

This galaxy ( $z = 0.0944$ ) shows a compact radio core, low surface brightness lobes and a hot-spot in the eastern lobe (Fig. 1p). With the jet length and width parameters from Table 5, we detect no X-ray emission other than in the core. The image seems to show a weak X-ray jet to the ENE that is only  $\sim 5''$  long but this emission is only marginally significant with  $P_{jet} = 0.080$ .

#### 1828+487 = 3C 380

The radio polarization electric vectors are parallel to the direction of the  $2''$ -long inner jet, oriented at a position angle of  $-40^\circ$ . A pc-scale superluminal radio jet (Polatidis & Wilkinson 1998) is aligned with this arcsec-scale jet. The *Chandra* point spread function is just small enough to provide a detection of a knot in the inner jet about  $1.8''$  from the core coincident with the inner radio jet (Fig. 1q). See also the X-ray and radio profiles (figs. 3 and 2).

#### 2052–474

This redshift 1.489 quasar has a bright radio core and a two-sided arcsec-scale radio jet (Fig. 1r). VLBA data on this object have not revealed the presence of a milliarcsec-scale jet (Tingay, Murphy, & Edwards 1998). We detect no extended X-ray emission.

#### 2101–490

2101–490 shows remarkably similar radio morphology to PKS 0637–752 (Fig. 1s). There is a long straight jet with three hotspots, after which the jet bends and terminates in a bright

lobe. The polarisation E-vectors remain orthogonal to the jet direction as far as the lobe where they are parallel. Several X-ray knots are also seen along the jet but unlike PKS 0637–752 they appear to be associated with areas of weak radio emission, and a knot exists past the bend. We have assigned a tentative redshift of 1.04 to 2101–490 based on a spectrum obtained at the Magellan telescope (Gelbord & Marshall 2004). New VLBI images show a jet about  $0.004''$  long at nearly the same position angle as inner part of the  $12''$  long jet (Ojha 2004).

#### 2251+158 = 3C 454.3

This redshift 0.859 quasar has a bright radio core and a one-sided arcsec-scale radio jet that was not intrinsically bright enough to be in the A subsample. A knot at the end of the jet is easily detected in the X-ray image (Fig. 1t). A pc-scale jet with components starting at a position angle  $-29^\circ$  and ending at a position angle of  $-80^\circ$  was detected in VLBI observations (Lobanov et al. 2000). VLBA data on this object shows a jet that curves from a position angle of  $-115^\circ$  to  $-60^\circ$  where it begins to align with the larger scale jet that is detected in X-rays.

## 4. DISCUSSION

The null hypothesis that bears testing with these data is that the jet is highly relativistic and aligned close to the line of sight so that the X-ray emission results from inverse Compton scattering of cosmic microwave background (IC-CMB) photons off jet electrons Celotti et al. (2001); Tavecchio et al. (2000). We have several lines of evidence that suggest that the jets in our sample are consistent with this interpretation.

### 4.1. Detection Statistics

We detect 12 new X-ray emitting jets among the 20 targets observed. Of these detections, 9 were in the A subsample of 10 sources, while only 3 were in just the B subsample. If detections were equally likely in both B and A samples, then the *a priori* probability that there would be  $< 4$  B detections would be 7.3%, so the hypothesis that the morphology selection is just as good as a flux selection remains tenable. Completing the *Chandra* imaging of these quasars may provide enough data to reject this hypothesis. Of the full sample of 56 sources, 19 of the A subsample have been observed using *Chandra* and 16 of these have jets that are detected in short exposures, for an 84% detection rate; the typical flux densities of detected jets are greater than 2 nJy. This detection rate is slightly higher than that obtained by Sambruna et al. (2004). The jet detection rate for the B-only subsample is not as high.

Fig. 6 shows that the B targets were generally fainter in the radio band, so that the limits on  $\alpha_{rx}$  were higher (i.e. fainter X-ray fluxes detected relative to the radio fluxes) than for the A targets. The B targets are mostly one-sided by selection, so, if sufficiently more B targets are detected in future observations to reject the hypothesis of similar A and B detection rates, then we would conclude that morphological selection yields sources with brighter X-ray jets, as might be expected if these are more closely aligned to the line of sight and are Doppler boosted.

### 4.2. Modeling the X-ray Emission

For a one population synchrotron model to extend from the radio to the X-ray band, the spectral index  $\alpha_{rx}$  would

have to be comparable to that in the radio band. If the radio spectral index is  $\alpha$ , then synchrotron models with a single power law distribution of electrons can be feasible if  $\alpha_{rx} \geq \alpha$  but then the optical flux would also be bright, so that  $\alpha_{rx} \geq \alpha_{ro} \geq \alpha$ . Our program of imaging using the Magellan telescope (Gelbord & Marshall 2004) places stringent limits on the optical emission from most X-ray emitting jets in the southern hemisphere, ruling out the single population synchrotron model.

Using the IC-CMB formulation given by Harris & Krawczynski (2002), we may obtain a crude estimate of the angle to the line of sight with some physical assumptions such as requiring that the magnetic field can be determined from the minimum energy argument. Harris & Krawczynski (2002) determined an expression for a combination of the bulk  $\Gamma$  and the angle to the line of sight,  $\theta$ , in terms of a few quantities derived from observables. Following their approach, for all jets in our sample, we first define  $B_1$ , the spatially averaged, minimum energy magnetic field in a jet in the case where there is no Doppler boosting ( $\Gamma = 1$ )

$$B_1 = \left[ \frac{18.85 C_{12} (1+k) L_s}{fV} \right]^{2/7} G \quad (1)$$

where  $\alpha = 0.8$ ,  $C_{12}$  is a weak function of  $\alpha$  and is  $5.7 \times 10^7$  for  $\alpha = 0.8$ , the filling factor is  $f = 1$ , the baryon energy fraction parameter  $k = 0$ , and the synchrotron spectrum (with index  $\alpha$ ) used to determine the synchrotron luminosity,  $L_s$ , (in  $\text{erg s}^{-1}$ ) extends from  $\nu_1 = 5 \times 10^6$  Hz to  $\nu_2 = 10^{15}$  Hz. The emission volume (in  $\text{cm}^3$ ) is estimated using the length of the jet as  $\theta_o - \theta_i$  and assuming a cylindrical cross section given by the diameter associated with the *Chandra* FWHM:  $0.75''$ . The filling factor is somewhat too large in general as most jets consist of a series of unresolved knots. The quantity  $B_1$  increases as  $f^{-2/7}$ , so  $B_1$  would increase by  $\times 1.6$  if  $f$  is as small as 0.2. The resultant magnetic fields are given in table 6.

Next, we compute  $R_1$ , the ratio of the synchrotron to inverse Compton luminosities. As long as both the radio and X-ray frequencies are far from the endpoints of the synchrotron and inverse Compton spectral breaks, then

$$R_1 \equiv \frac{S_x(\nu/\nu_x)^{-\alpha}}{S_r(\nu/\nu_r)^{-\alpha}} = \frac{S_x \nu_x^\alpha}{S_r \nu_r^\alpha} = (\nu_x/\nu_r)^{\alpha - \alpha_{rx}}, \quad (2)$$

where  $\nu_r$  and  $\nu_x$  are the radio and X-ray frequencies at which the flux densities  $S_x$  and  $S_r$  are observed. We then compute the quantity

$$K = B_1 (aR_1)^{1/(\alpha+1)} (1+z)^{-(\alpha+3)/(\alpha+1)} b^{(1-\alpha)/(\alpha+1)}, \quad (3)$$

where  $a = 9.947 \times 10^{10} \text{ G}^{-2}$  and  $b = 38080 \text{ G}$  are constants and  $B_1$  is expressed in G, so  $K$  is dimensionless. For  $\Gamma \gg 1.5$ , then  $\Gamma^{\alpha+1} \gg \frac{\Gamma^{\alpha-1}}{4}$ , so we may use eq. A24 from Harris & Krawczynski (2002):

$$K = \Gamma \delta (1 + \mu'_j) = \frac{1 - \beta + \mu - \mu\beta}{(1 - \mu\beta)^2}, \quad (4)$$

where we have substituted the equation for the cosine of the angle to the line of sight in the jet frame,  $\mu'_j$ , with the angle transformation formula  $\mu' = \frac{\mu - \beta}{1 - \mu\beta}$  and the formula for the Doppler factor  $\delta = [\Gamma(1 - \mu\beta)]^{-1}$  and rearranged. We solve

eq. 4 for  $\mu$  to obtain the angle to the line of sight for any value of  $K$  and an allowable value of  $\beta$ :

$$\mu = \frac{1 - \beta + 2K\beta - (1 - 2\beta + 4K\beta + \beta^2 - 4K\beta^3)^{1/2}}{2K\beta^2}, \quad (5)$$

By assuming that all the observed quasar jets have the same  $\Gamma = 1/(1 - \beta^2)^{1/2} = 10$ , then we find that the jets have angles  $\theta$  to the line of sight as given in table 6. Limits are given for jets that are not detected in X-rays. The angles are rather robust to many of the assumed physical parameter. For example,  $\theta$  decreases 10% if  $B_1$  increases 60% ( $B_1$  includes the estimate of the volume and filling factor, see eq. 1), increases 15% if  $\nu_2$  decreases to  $10^{11}$  Hz, and drops 15% if  $\alpha$  is decreased to 0.70. The angles range from  $9^\circ$  to over  $40^\circ$ . The values for the FR I radio galaxy, 1343–601, are not realistic because the jet is not likely to be relativistic, so eq. 4 wouldn't apply. These angles are meant only to be indicative for the remaining jets; better models would be obtained by fitting the spectra of individual knots within the jets. In this model, where  $\gamma = 10$  is assumed, the angles determined for the jets are generally small, often less than  $20^\circ$ . Small angles to the line of sight are expected due to the sample selection (e.g., most are flat-spectrum, core-dominated radio sources). Some of the cores show relativistic jets in VLBI images; these would be apparently brighter than quasars with jets perpendicular to the line of sight and more likely to populate the parent flux-limited sample. The jet angle distribution depends on the assumed value of  $\Gamma$ , which may also be distributed, so we have chosen a value which is close to the median of values determined from VLBI observations of quasar cores.

Another potentially important possible source of variance is in the detailed shape of the electron energy distribution. Because the radio band results from radiation by a different set of particles than produces the X-ray emission in this model, the derived beaming parameters would change if electron number densities do not follow the power law model. We can estimate the radio frequency,  $\nu_s$ , where the electrons dominate the synchrotron radiation spectrum that upscatter CMB photons into the X-ray band to energies of  $h\nu_{IC} = 1 \text{ keV}$ . Starting from eq. B2 of Harris & Krawczynski (2002):

$$\nu_s = \frac{\nu_{IC} B'}{b\Gamma(1+z)(1 + \mu'_j)} \quad (6)$$

where  $B' = B/\delta$  is the magnetic field in the rest frame. Then, using eqs. 3 and 4, we find a simple relation between the ratio of the synchrotron and IC frequencies, depending only on the luminosity ratio,  $R_1$ :

$$\frac{\nu_s}{\nu_{IC}} = \left[ \frac{(1+z)^2}{ab^2 R_1} \right]^{\frac{1}{\alpha+1}} \quad (7)$$

Values of  $\nu_s$  were determined for each source and are given in Table 6. All values are between 5 and 35 MHz, which is well below the frequencies of the radio maps we use to measure the knots (but above the synchrotron cutoff used to determine the synchrotron luminosity).

In the IC-CMB model, the X-ray flux increases as the local energy density in the CMB increases with redshift. From eq. 4, we expect  $R_1 \propto (1+z)^{3+\alpha}$ . In Fig. 7, we show the measurements and limits on  $\alpha_{rx}$  as a function of  $(1+z)$ , where we set  $z = 1$  for the source without a measured redshift. If the IC-CMB model were the dominant mechanism for determining

the X-ray flux, one might expect to find smaller values of  $\alpha_{rx}$  at high  $z$ . No such trend is indicated in the data, which might just indicate that other factors dominate the distribution of  $\alpha_{rx}$  such as angles to the line of sight and bulk  $\Gamma$ . The distribution of  $\alpha_{rx}$  at any given redshift can be quite broad, corresponding to a range in  $R_1$  of over a factor of 40 near  $z = 0.8$ .

There were no X-rays detected from counter-jets. This result is consistent with the IC-CMB hypothesis, where X-ray emission would only be observed from the approaching jet due to Compton scattering into the line of sight. Consider the ratio,  $\xi$ , of  $R_1$  for a receding jet to that of an oppositely pointed, similar velocity approaching jet. This ratio can be determined from equations 3 and 4 by reversing the sign of  $\mu$ :

$$\xi \equiv \frac{R_1^+}{R_1^-} = \left[ \frac{1-\mu}{1+\mu} \left( \frac{1-\mu\beta}{1+\mu\beta} \right)^{2\gamma} \right]^{1+\alpha} \quad (8)$$

The quantity  $\mu$  is defined to be positive for the approaching jet and using  $\beta < 1$ , it is easy to show that that  $\xi < 1$  for all choices of  $\mu$  and  $\beta$ . Thus, the inverse Compton X-ray emission from a relativistic counterjet will always be weaker relative to the radio emission than for the approaching jet.

Detailed analysis of several of the brighter quasar jets shows that even the meager data for some of the knots already require large beaming factors and small angles to the line of sight. Schwartz et al. (2003) and Schwartz et al. (2004) used the spatially resolved radio/X-ray SEDs of four sources from this sample to measure magnetic fields and relativistic beaming factors as a function of distance along the jet, and inferred the kinetic powers and radiative efficiencies of the jets. The minimum energy magnetic fields are estimated from the radio fluxes and approximate values for the angular diameters of the knots. As expected, Schwartz et al. (2004) found that the high X-ray fluxes required can be explained reasonably well in the IC-CMB model. The rest frame magnetic fields of the differ-

ent jets were of order 10 to 20  $\mu\text{G}$ ; our values are generally smaller, 4-14  $\mu\text{G}$ , due to the larger regions used. The measured beaming factors of 2.5 to 10.6 indicate that the jet axes must be within 5 to 25° of our line of sight, while we find angles of 15 to 28° for these same sources using the total jet flux densities. The kinetic powers are of the same order as the core luminosities for these jets, and their radiative efficiencies are  $\sim 1\%$  or less. Deeper observations will improve the analysis of individual knots in these jets and provide an opportunity to test the IC-CMB model better by providing a measure of the X-ray spectra and perhaps additional knot detections.

We thank Brendan Miller, Jeff Bridgham, Chris Copperwheat, and Martin Terry for their contributions to the analysis at an early stage. Support for this work was provided by the National Aeronautics and Space Administration (NASA) through Chandra Award Number NAG 5-10032 issued by the Chandra X-Ray Center (CXC), which is operated by the Smithsonian Astrophysical Observatory for and on behalf of NASA under contract NAS 8-39073. HLM was supported under NASA contract SAO SV1-61010 for the CXC. DAS was partially supported by Chandra grant G02-3151C to SAO from the CXC. JMG was supported under Chandra grant G02-3151A to MIT from the CXC. This research has made use of the United States Naval Observatory Radio Reference Frame Image Database. The Australia Telescope Compact Array is part of the Australia Telescope which is funded by the Commonwealth of Australia for operation as a National Facility managed by CSIRO. This research has made use of the NASA/IPAC Extragalactic Database (NED) which is operated by the Jet Propulsion Laboratory, California Institute of Technology, under contract with the National Aeronautics and Space Administration.

## REFERENCES

- Baum, S. A. & Heckman, T. 1989, *ApJ*, 336, 702  
 Beasley, A. J., Gordon, D., Peck, A. B., Petrov, L., MacMillan, D. S., Fomalont, E. B., & Ma, C. 2002, *ApJS*, 141, 13  
 Birkinshaw, M., Worrall, D. M., & Hardcastle, M. J. 2002, *MNRAS*, in press  
 Birkinshaw, M., 1994, *ASP Conference Series*, Vol. 61, ed. D.R. Crabtree, R.J. Hanisch, J. Barnes, page 249  
 Celotti, A., Ghisellini, G., and Chianberge, M. 2001, *MNRAS*, 321, L1  
 Davis, J.E., 2001, *ApJ*, 562, 575  
 Dickey, J.M., Lockman, F.J. 1990, *ARAA*, 28, 215  
 Elvis, M., Lockman, F.J., Wilkes, B.J. 1989, *AJ*, 97, 777  
 Fomalont, E. B., Frey, S., Paragi, Z., Gurvits, L. I., Scott, W. K., Taylor, A. R., Edwards, P. G., & Hirabayashi, H. 2000, *ApJS*, 131, 95  
 Fossati, G., Maraschi, L., Celotti, A., Comastri, A., Ghisellini, G. 1998, *MNRAS*, 299, 433  
 Gambill, J.K., Sambruna, R.M., Chartas, G., Cheung, C.C., Maraschi, L., Tavecchio, F., Urry, C.M., Pesce, J.E. 2003, *A&A*, 401, 505  
 Gelbord, J.M. and Marshall, H.L. 2004, in preparation  
 Hardcastle, M. J., Birkinshaw, M., & Worrall, D. M. 2001a, *MNRAS*, 323, L17  
 Hardcastle, M. J., Birkinshaw, M., & Worrall, D. M. 2001b, *MNRAS*, 326, 1499  
 Hardcastle, M. J., Worrall, D. M., Kraft, R. P., Forman, W. R., Jones, C., & Murray, S. S. 2003, *ApJ*, 593, 169  
 Harris, D.E., et al. 2000, *ApJ*, 530, L81  
 Harris, D. E. & Krawczynski, H. 2002, *ApJ*, 565, 244  
 Kraft, R. P., Forman, W. R., Jones, C., Murray, S. S., Hardcastle, M. J., & Worrall, D. M. 2002, *ApJ*, 569, 54  
 Kubo, H., Takahashi, T., Madejski, G., Tashiro, M., Makino, F., Inoue, S., Takahara, F. 1998, *ApJ*, 504, 693  
 Lobanov, A. P., et al. 2000, *A&A*, 364, 391  
 Lovell, J. 1997, Ph.D. Thesis, U. of Tasmania  
 Lovell, J.E.J., et al. 2000, *Astrophysical Phenomena Revealed by Space VLBI*, eds. H. Hirabayashi, P.G. Edwards, and D.W. Murphy, p. 215  
 Marshall, H.L., et al. 2001, *ApJ*, 549, L167  
 Marshall, H. L., Miller, B. P., Davis, D. S., Perlman, E. S., Wise, M., Canizares, C. R., & Harris, D. E. 2002, *ApJ*, 564, 683  
 Murphy, D.W., Browne, I.W.A., and Perley, R.A. 1993, *MNRAS*, 264, 298  
 Murphy, E.M., Lockman, F.J., Laor, A., Elvis, M. 1996, *ApJS*, 105, 369  
 Ojha, R. 2004, private communication  
 Pesce, M. J., et al. 2002, *ApJ*, 556, 79  
 Polatidis, A. G. & Wilkinson, P. N. 1998, *MNRAS*, 294, 327  
 Prieto, M.A., 1996, *MNRAS*, 282, 421  
 Rawlings, S. & Saunders, R. 1991, *Nature*, 349, 138  
 Reeves, J.N., Turner, M. J.L. 2000, *MNRAS*, 316, 234  
 Sambruna, R. M. 1997, *ApJ*, 487, 536  
 Sambruna, R. M., Maraschi, L., Tavecchio, F., Urry, C. M., Cheung, C. C., Chartas, G., Scarpa, R., & Gambill, J. K. 2002, *ApJ*, 571, 206  
 Sambruna, R. M., Gambill, J.K., Maraschi, L., Tavecchio, F., Cerutti, R., Cheung, C. C., Urry, C. M., & Chartas, G., 2004, *ApJ*, in press  
 Schwartz, D.A., et al. 2000, *ApJ*, 540, L69  
 Schwartz, D. A. et al. 2003, *New Astronomy Review*, 47, 461  
 Schwartz, D.A., et al. 2004, *ApJ*, submitted  
 Tavecchio, et al. 2000, *ApJ*, 544, L23  
 Tavecchio, F., et al. 2002, *ApJ*, 575, 137  
 Tingay, S. J., Murphy, D. W., & Edwards, P. G. 1998, *ApJ*, 500, 673  
 Tingay, S. J. et al. 2002, *ApJS*, 141, 311  
 Wilson, A. S. & Yang, Y. 2002, *ApJ*, 568, 133  
 Worrall, D.M., in *AGN and the X-ray Background, Proceedings of the 23rd ESLAB Symposium, Bologna*, ESA SP-296 (ESA Publications), 719  
 Worrall, D. M., Birkinshaw, M., & Hardcastle, M. J. 2001, *MNRAS*, 326, L7.

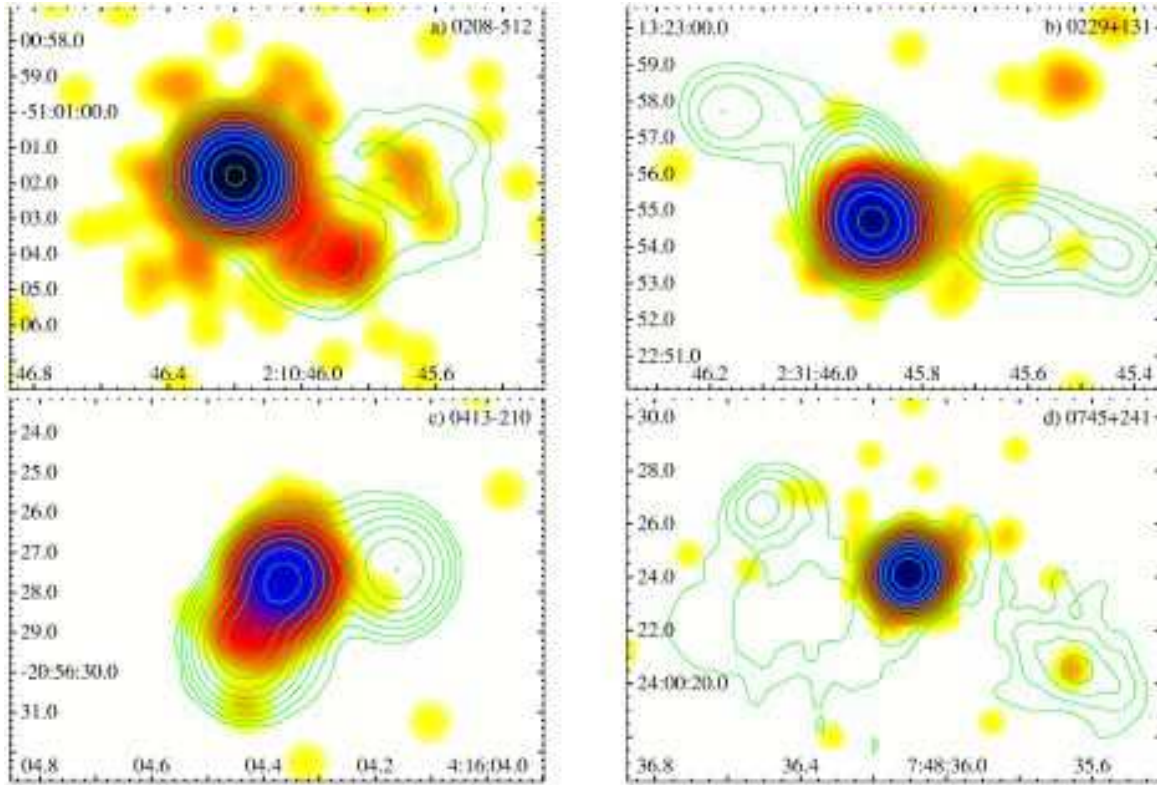


FIG. 1.— X-ray images obtained with the Chandra X-ray Observatory, overlaid by contours of radio emission obtained at the Australia Telescope Compact Array or the Very Large Array (VLA). The images appear in the following order: *a)* 0208–512, *b)* 0229+131, *c)* 0413–210, *d)* 0745+241, *e)* 0858–771, *f)* 0903–573, *g)* 0920–397, *h)* 1030–357, *i)* 1046–409, *j)* 1145–676, *k)* 1202–262, *l)* 1258–321, *m)* 1343–601, *n)* 1424–418, *o)* 1655+077, *p)* 1655–776, *q)* 1828+487, *r)* 2052–474, *s)* 2101–490, and *t)* 2251+158. The flux densities increase by  $\times 2$  for each radio contour, starting at a value of five times the rms noise. Two images are shown with extra contours (in red): PKS 1030–357 (Fig. 1h) includes two contours from a lower-frequency radio map (at  $5\times$  and  $10\times$  the rms level) to illustrate larger-scale structures, and PKS 1343–601 (Fig. 1m) adds an extra contour at  $3\times$  the rms level to emphasize the diffuse structure. The synthesized radio Gaussian beamsizes are convolved to produce circular  $1.2''$  FWHM beams in all images. Radio contour details are provided in Table 3. The X-ray images are convolved with Gaussians to match the radio beamsizes and then binned at  $0.0492''$ . The color scales are the same in all images, ranging logarithmically from 0.5 counts/beam (yellow) to 2500 counts/beam (black). Notes on individual objects are given in the text.

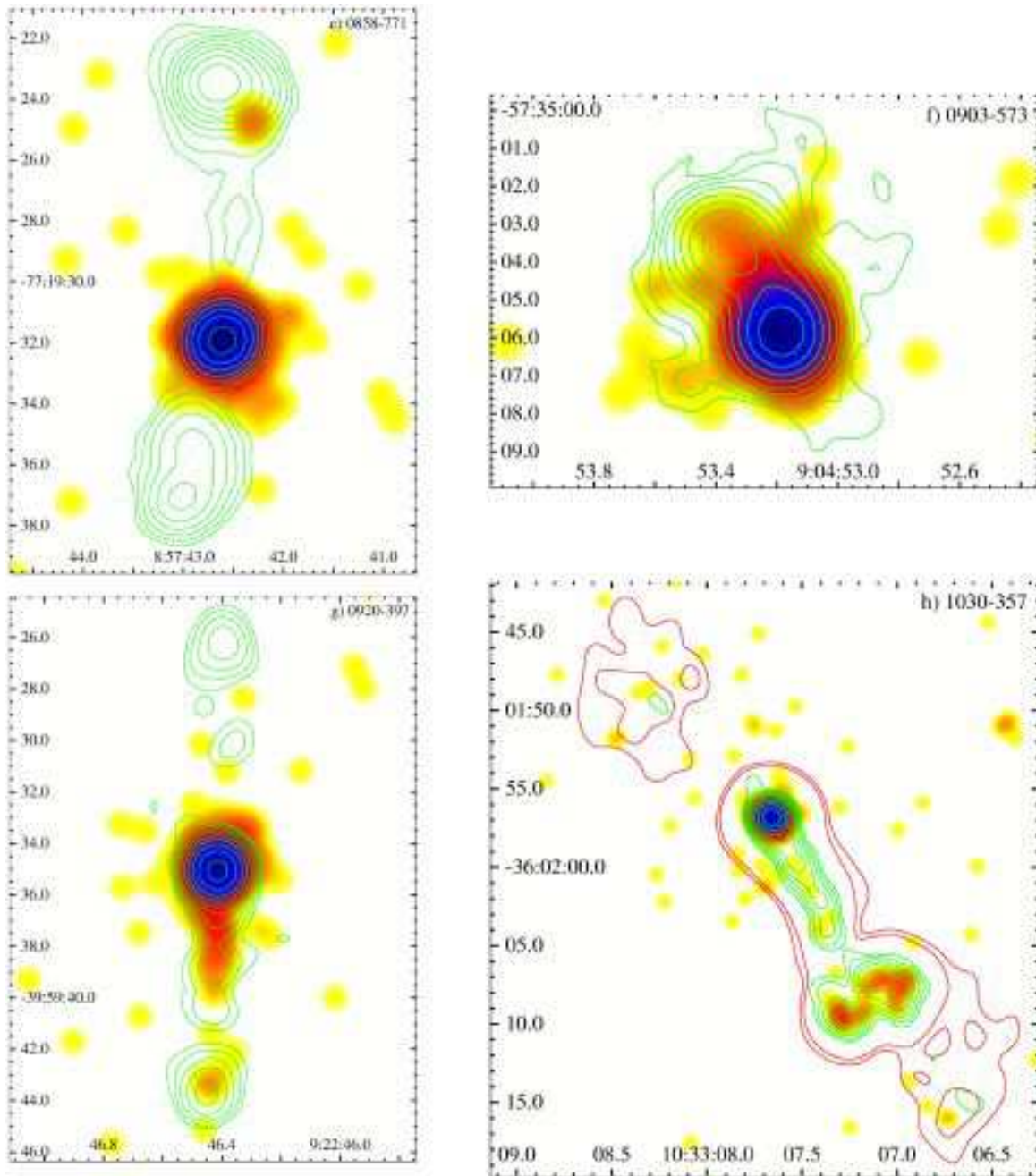


FIG. 1.— continued.

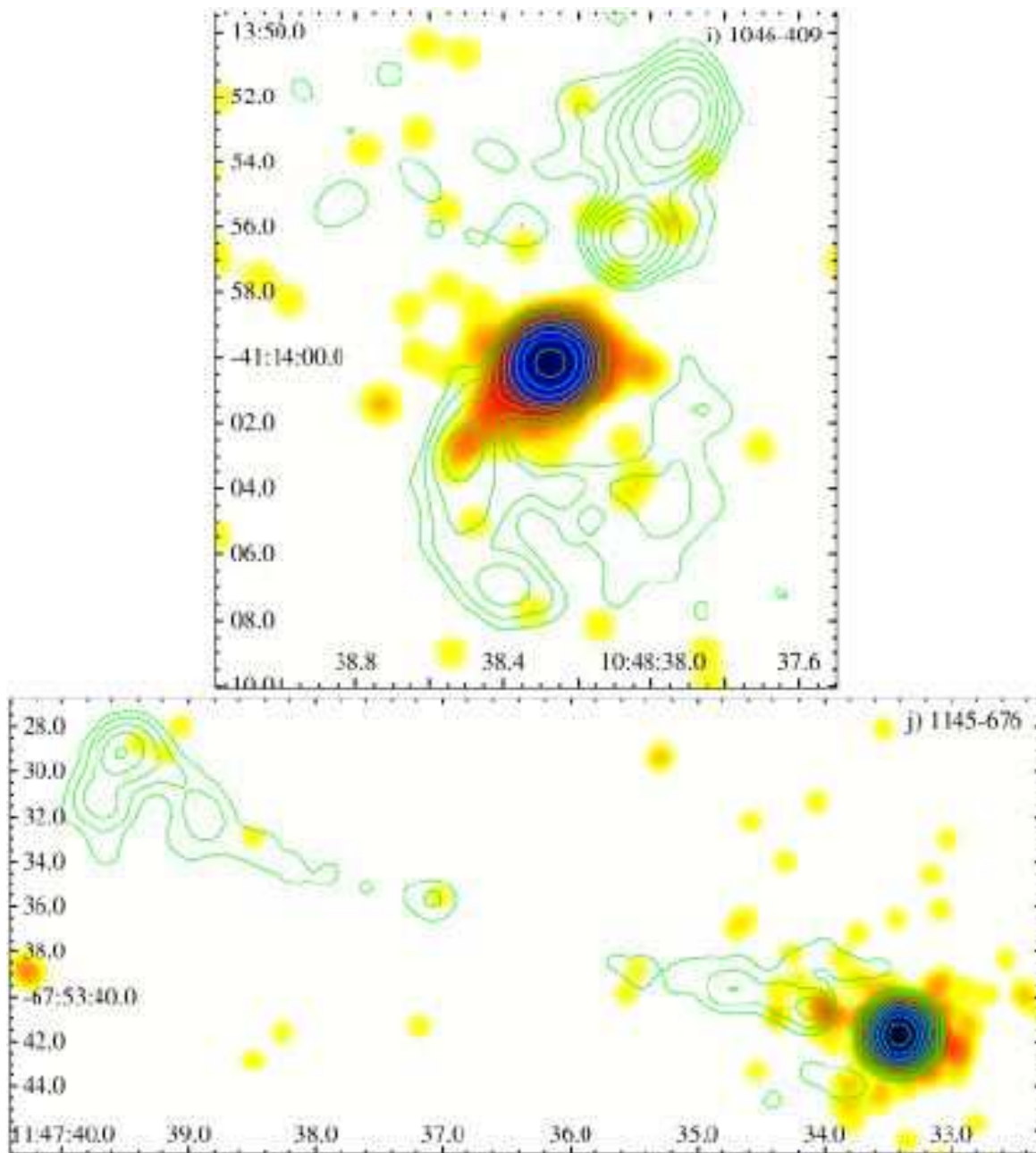


FIG. 1.— continued.

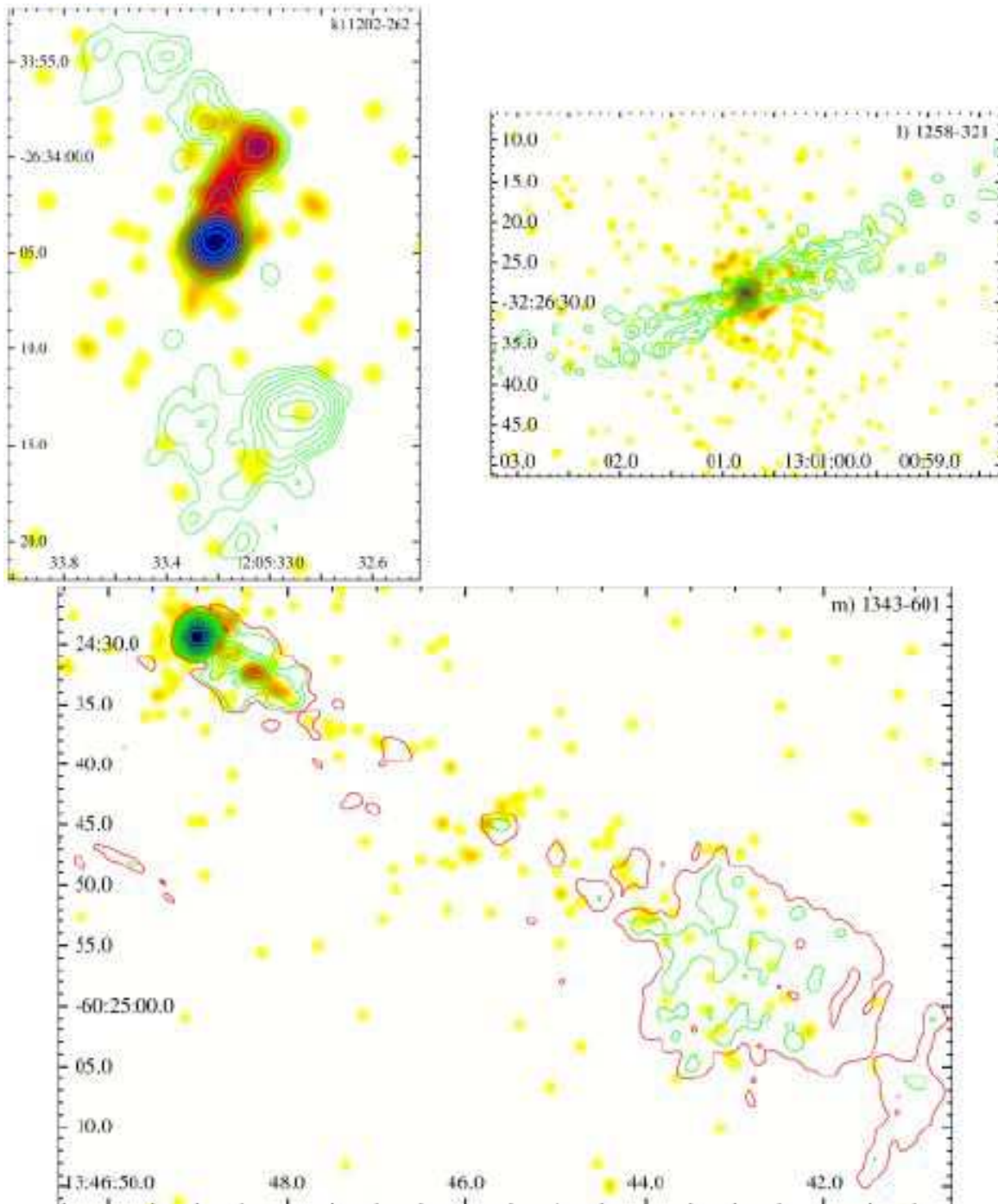


FIG. 1.— continued.

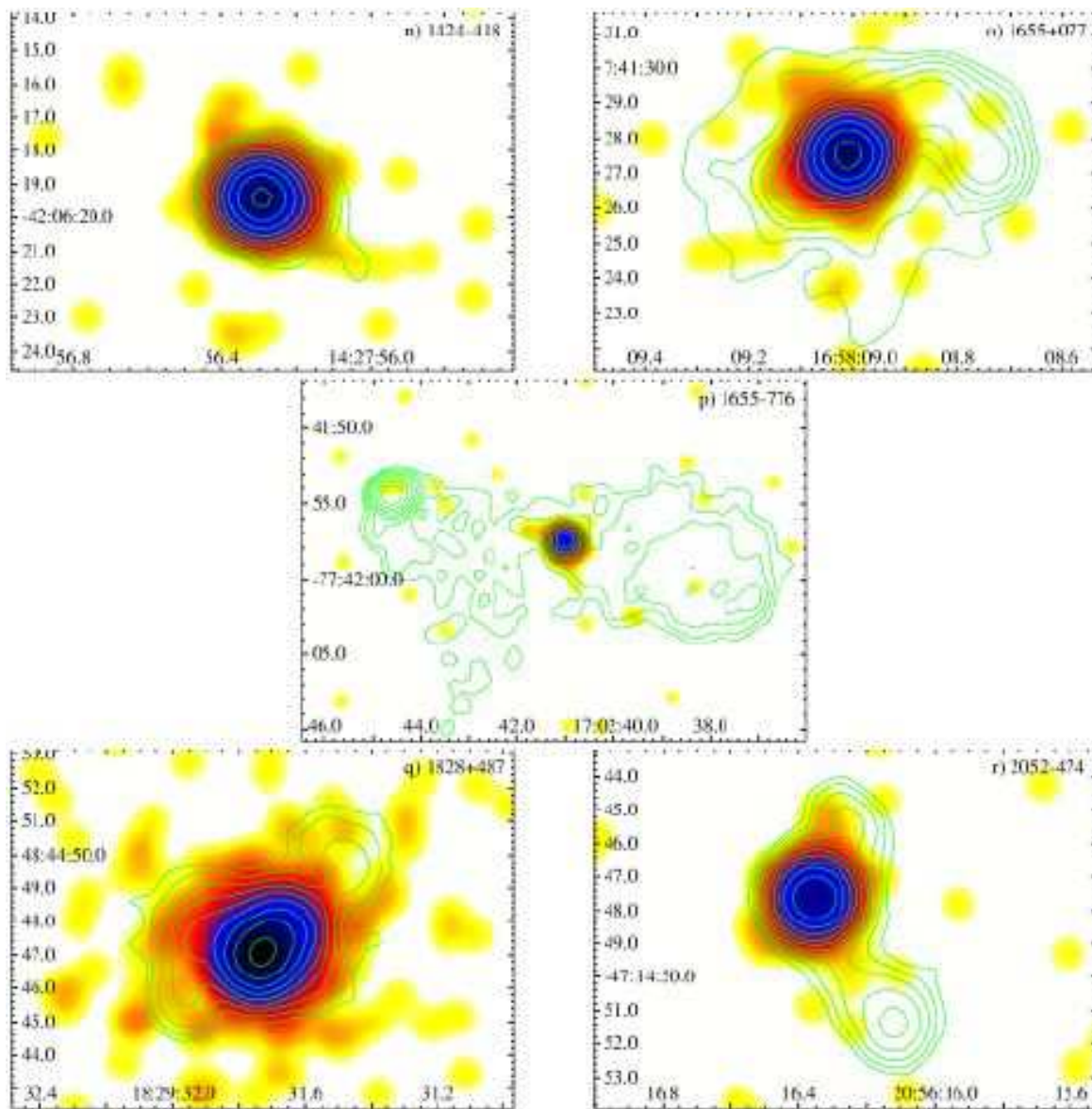


FIG. 1.— continued.

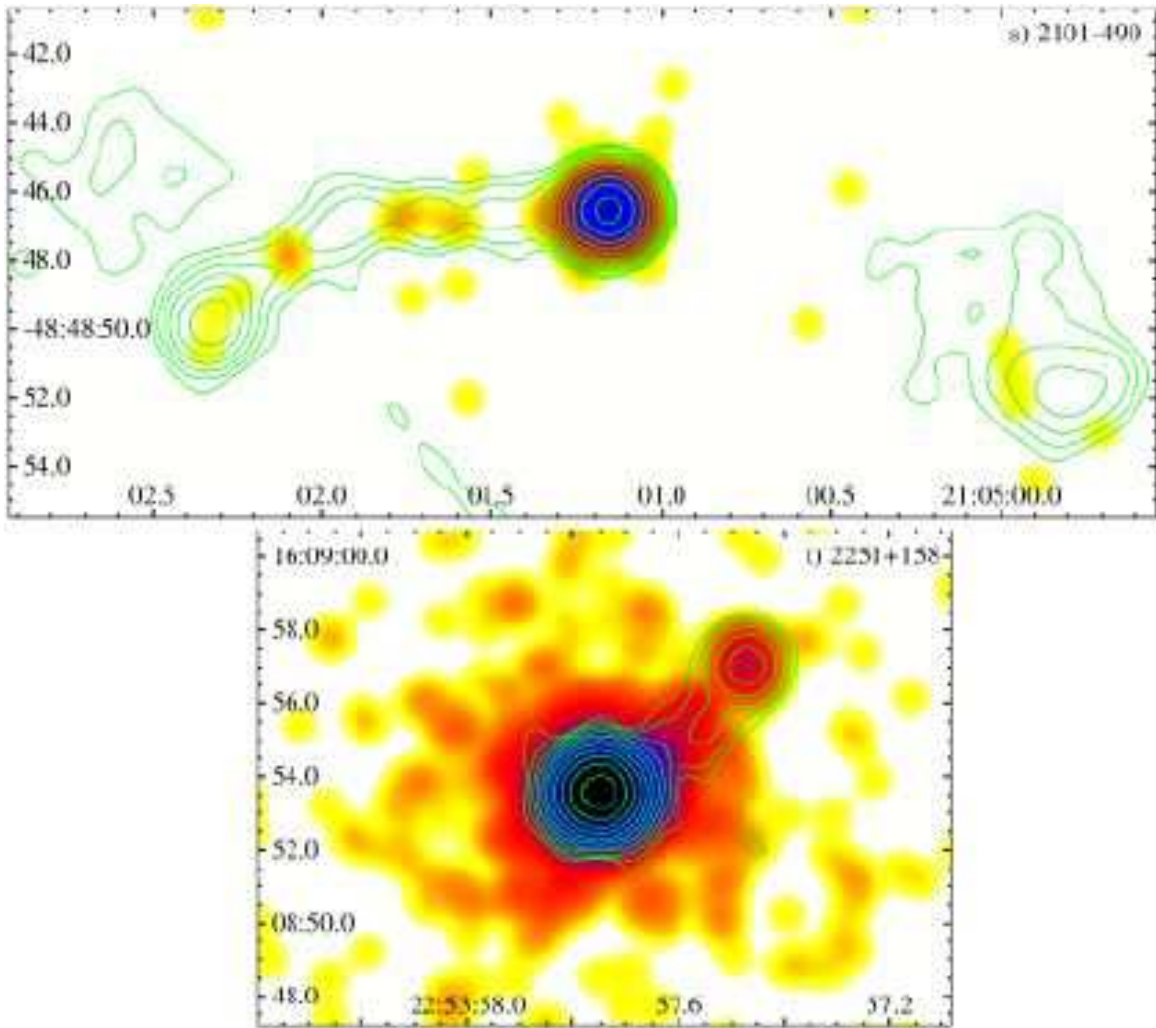


FIG. 1.— continued.

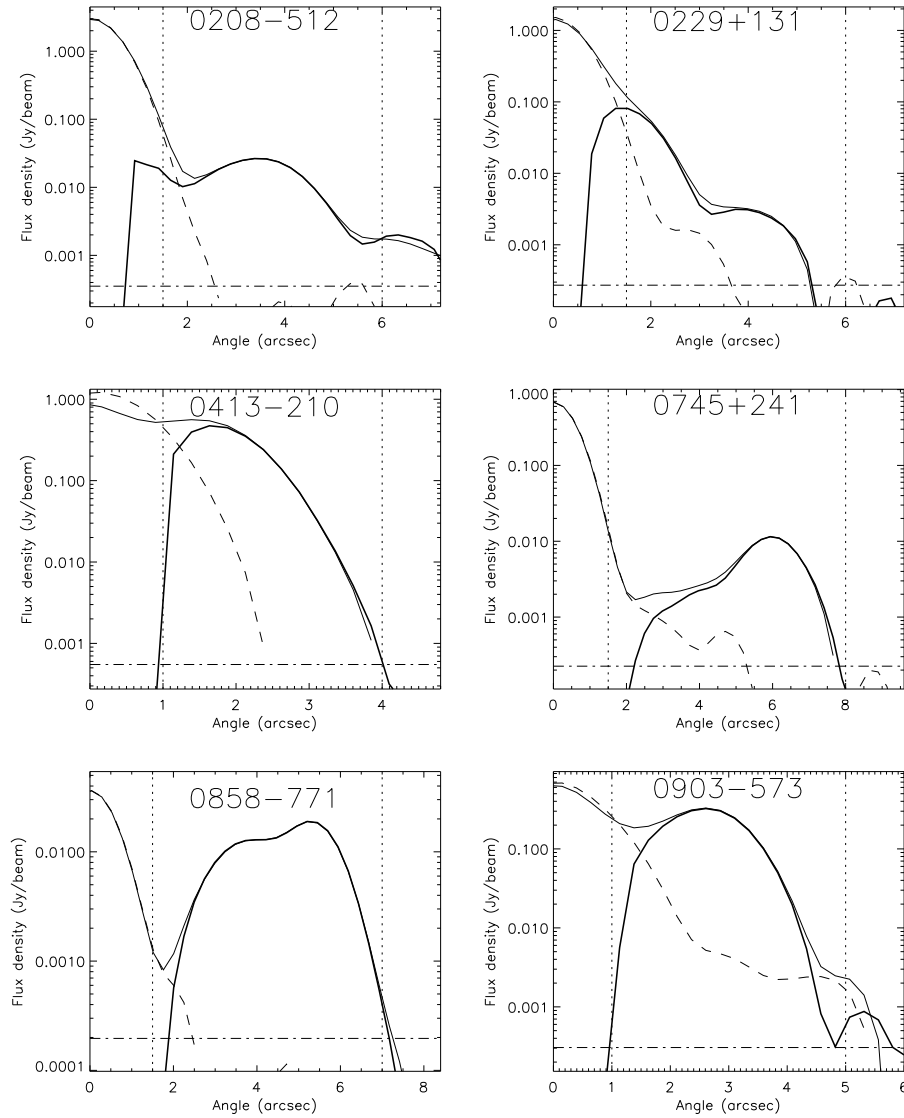


FIG. 2.— Profiles of the radio images. The solid, thin lines give the profiles along the position angles of the jets, as defined in Table 5 and used for measuring the X-ray profiles. The counts are determined in rectangles  $3''$  wide, except for 1030–357 and 2101–490, where the jets bend substantially, so the rectangles were widened to  $10''$  and  $5''$ , respectively. The dashed lines give the profiles at a position angle  $90^\circ$  CW from the jet to avoid any counter-jets or lobes opposite the jet. The solid, bold lines give the difference between the profiles along the jet and perpendicular to it, so that the core is effectively nulled and the jet flux can be measured as a residual between the vertical dotted lines. The horizontal dash-dot lines give the average noise level in the map.

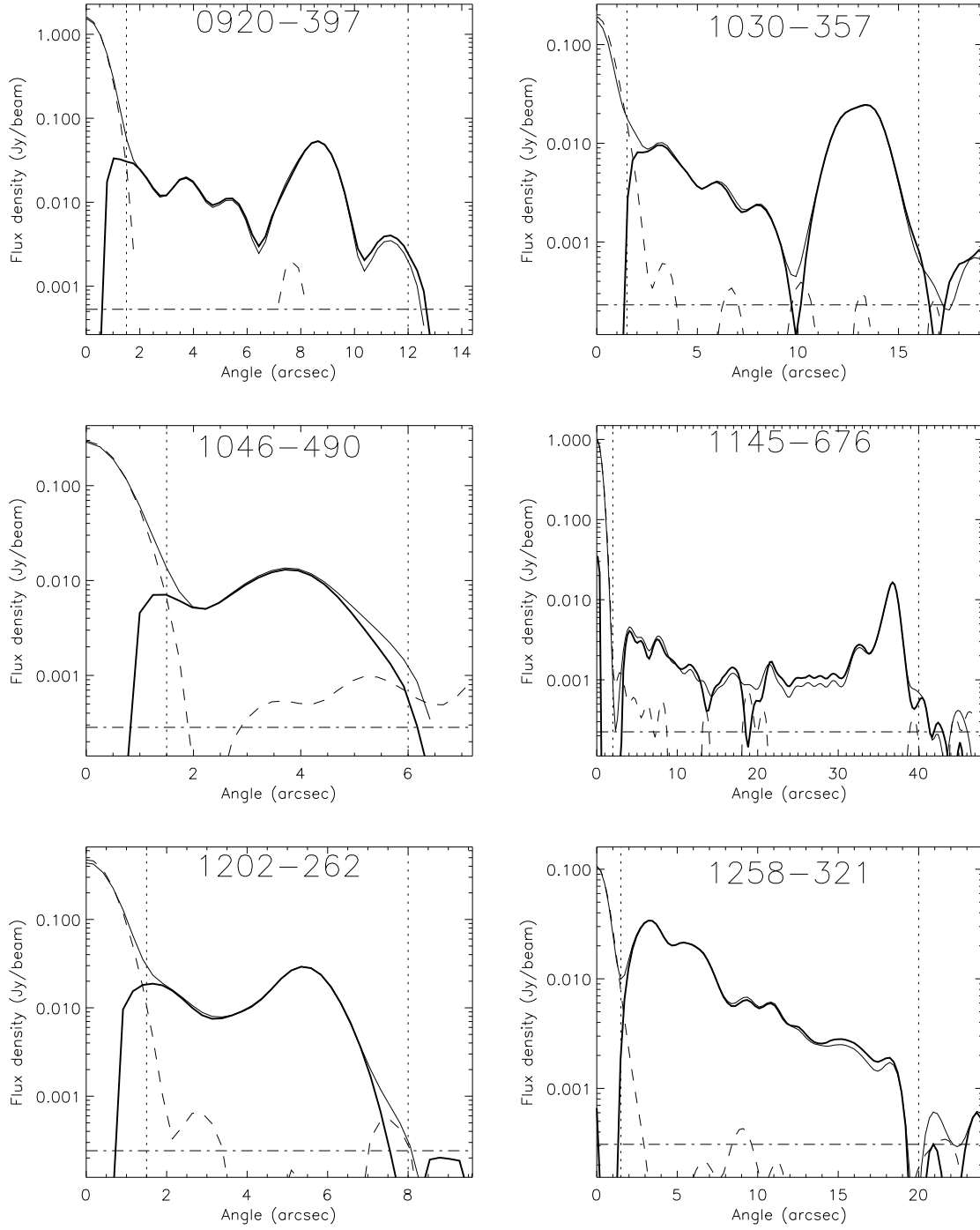


FIG. 2.— continued.

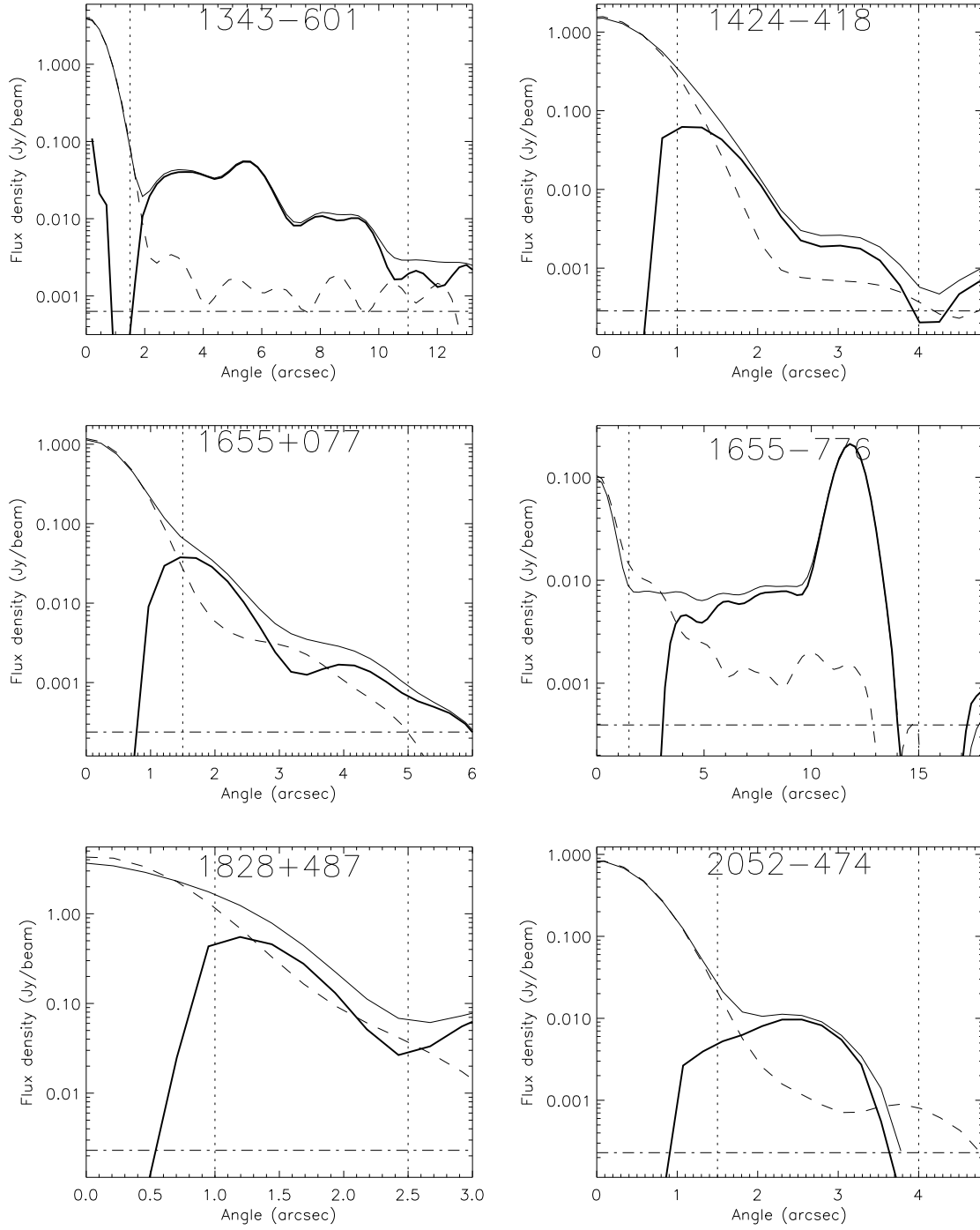


FIG. 2.— continued.

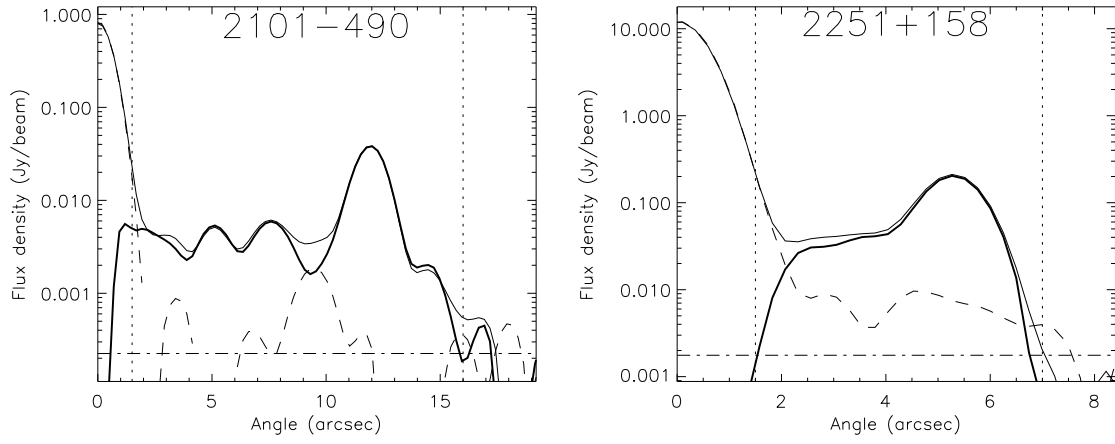


FIG. 2.— continued.

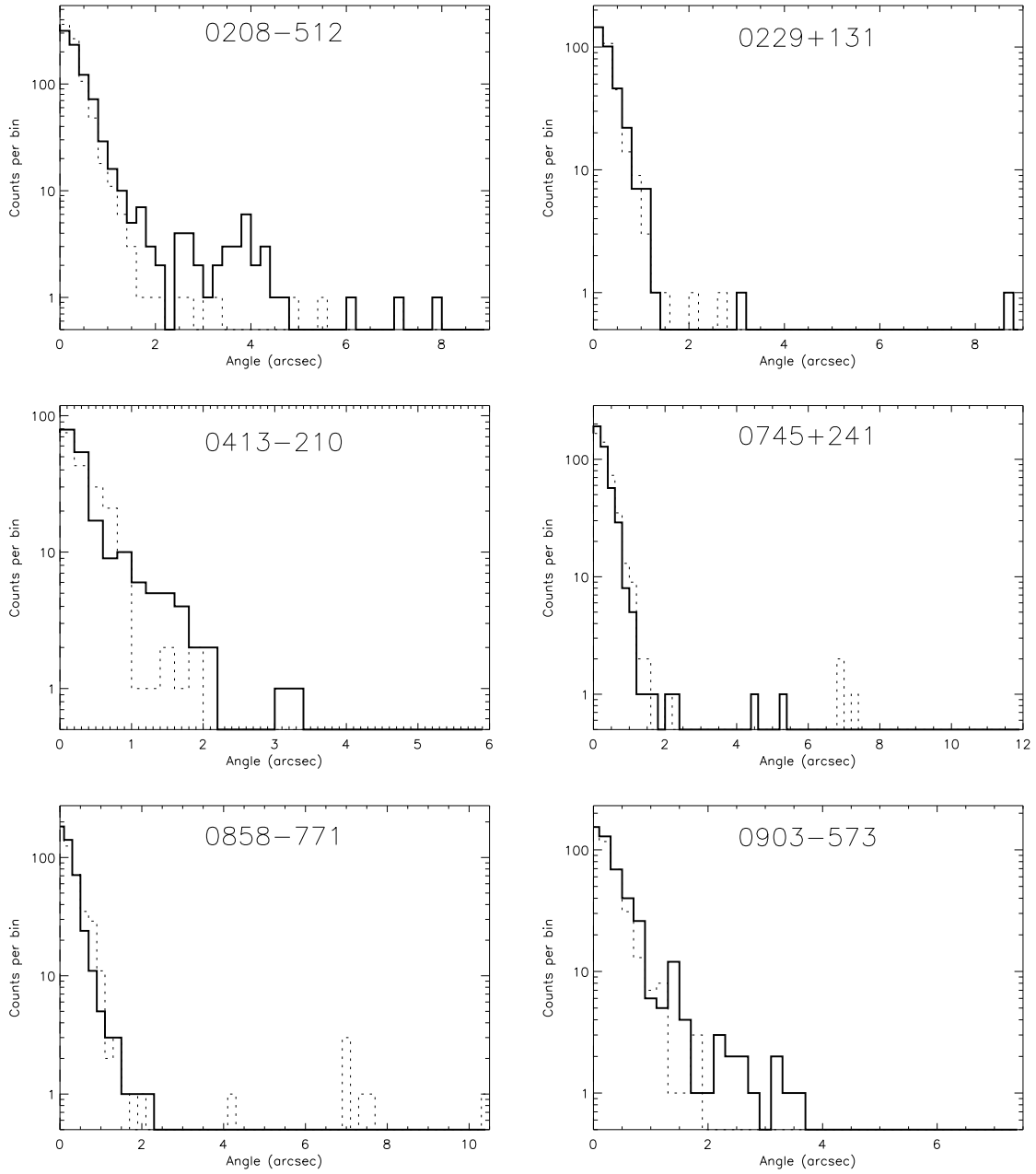


FIG. 3.— Histograms of counts from the X-ray images in  $0.2''$  bins. The solid, bold lines give the profiles along the position angles of the jets, as defined in Table 5 and used in Fig. 2. The dashed histograms give the profiles at a position angle  $180^\circ$  opposite to the jet – the counter-jet direction. The counter-jet profiles provide a measure of the significance of the X-ray emission from the jet because there are no clearly detected counter-jets.

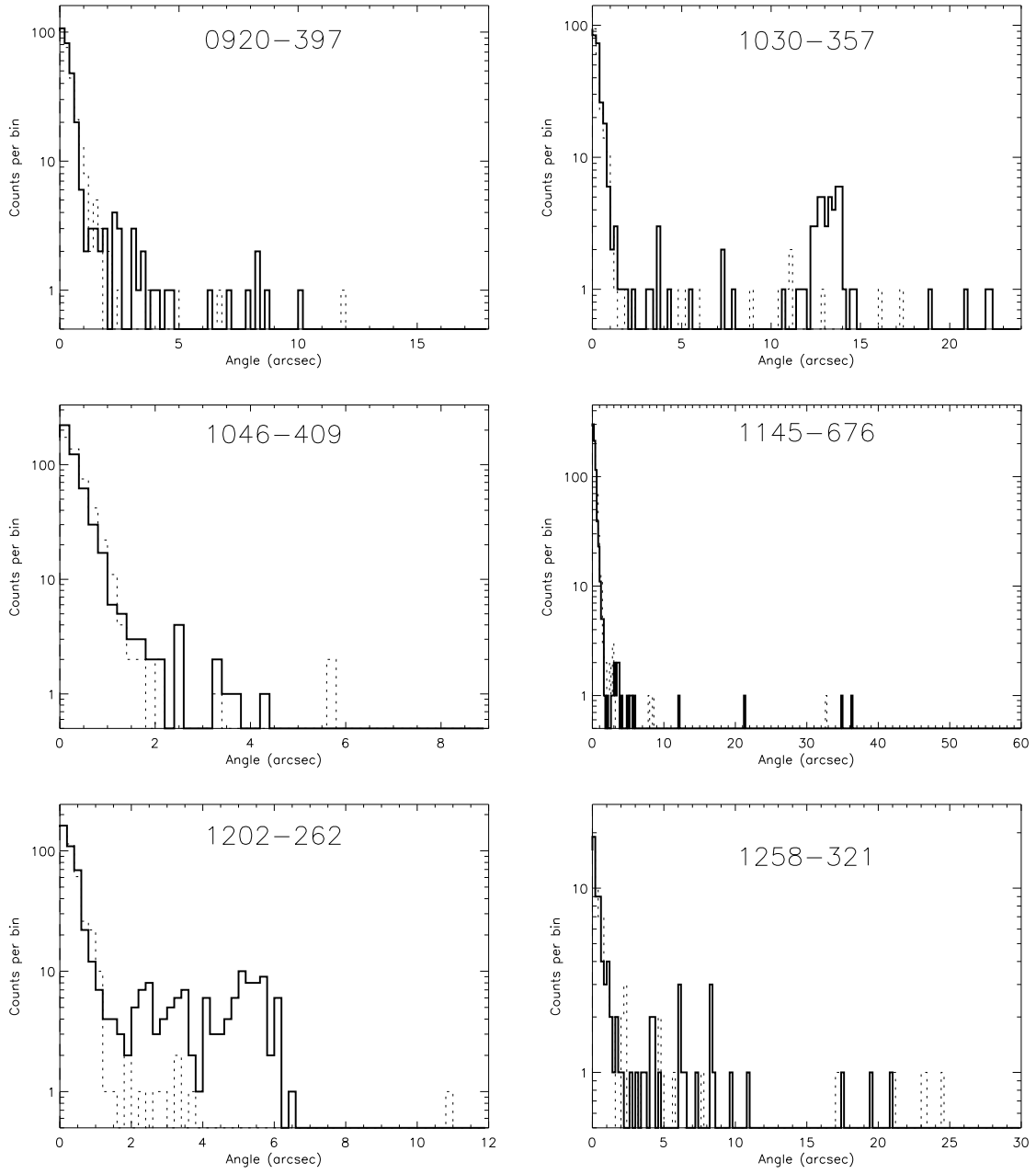


FIG. 3.— continued.

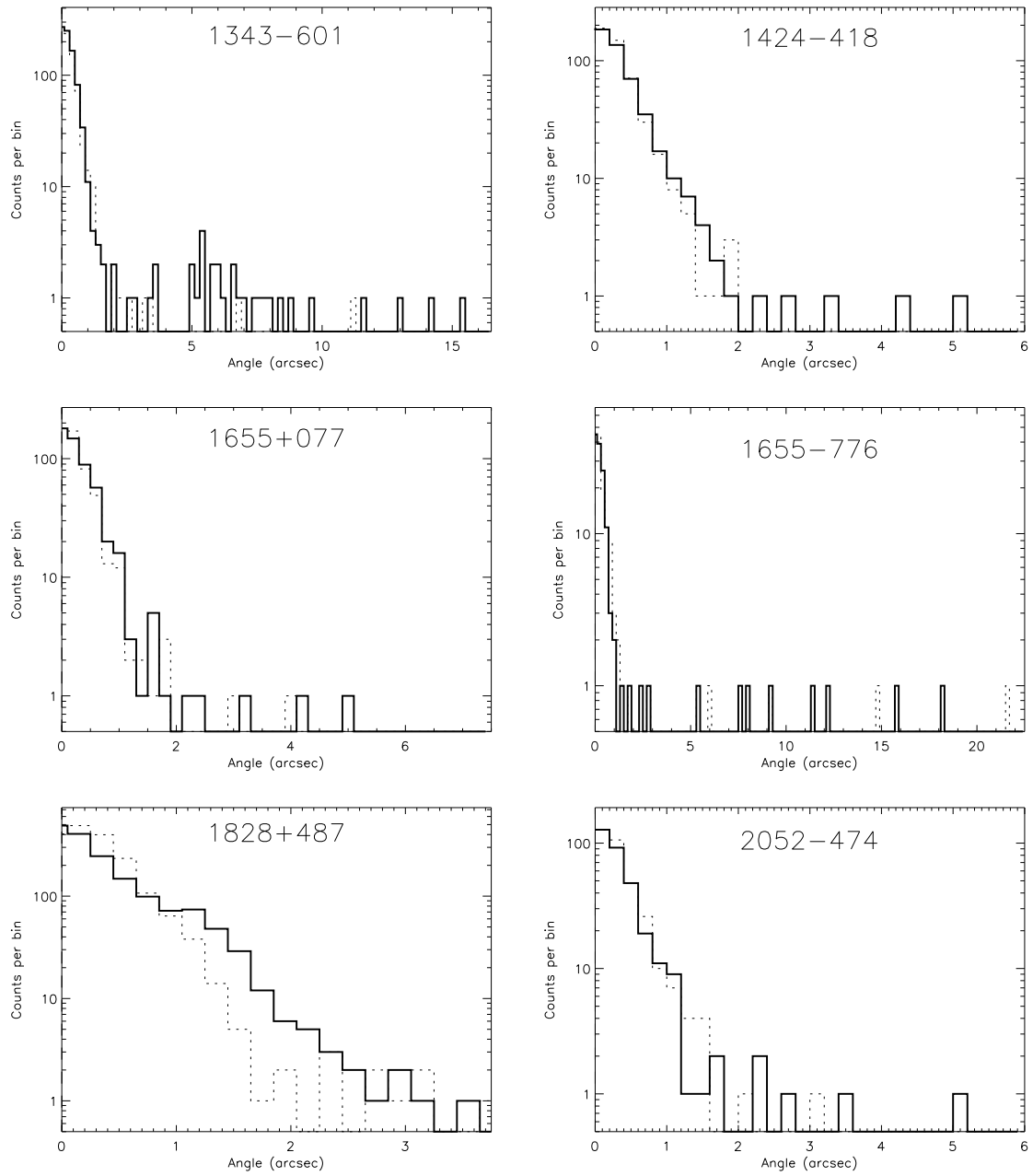


FIG. 3.— continued.

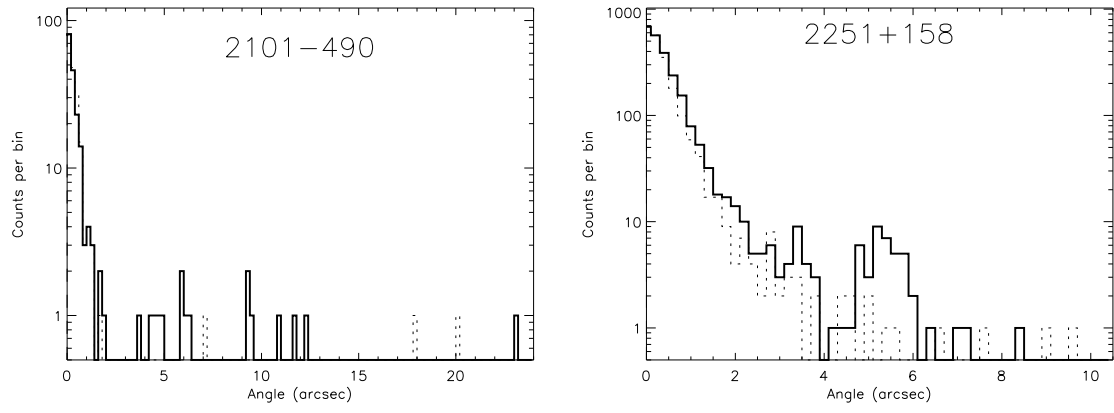


FIG. 3.— continued.

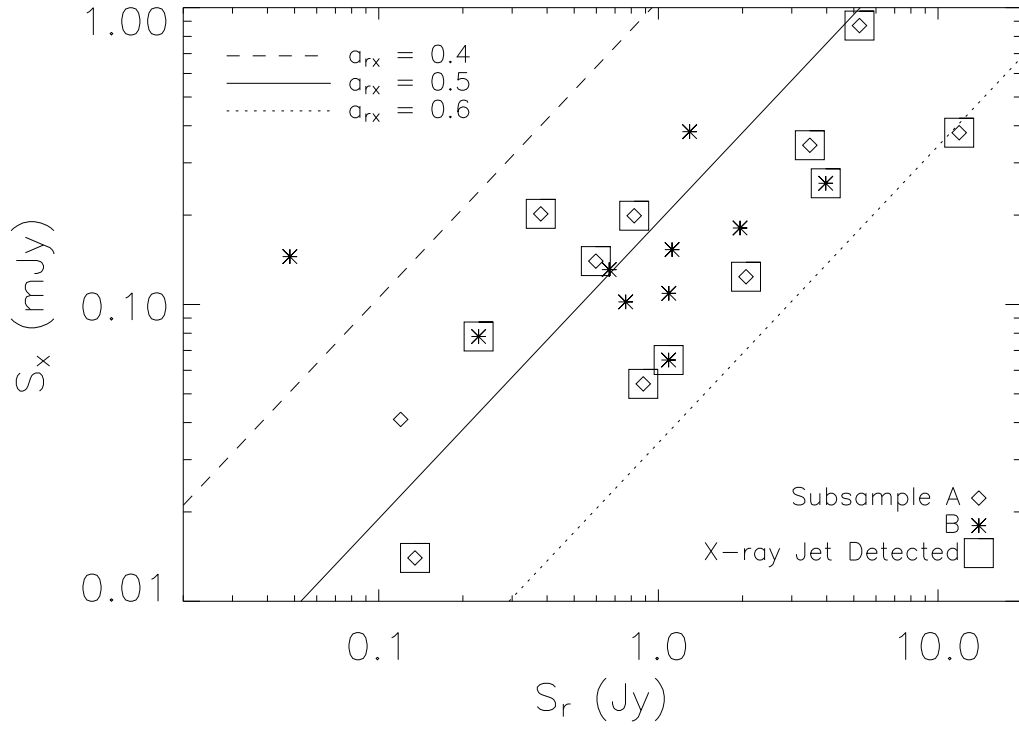


FIG. 4.— X-ray and radio flux densities for the cores of the targets in the observation set. The radio flux densities were measured from the maps shown in Fig. 1 and then adjusted to 5 GHz assuming  $\alpha_r = 0.5$ . The X-ray flux densities are estimated at 1 keV ( $2.42 \times 10^{17}$  Hz). Error bars in either flux density are generally small —  $\lesssim 10\%$ . The A and B targets have similar distributions. The spectral indices from the radio to the X-ray band ( $\alpha_{rx}$ ) cluster about a value of 0.5. Similarly, jets are detected without bias regarding either this spectral index or the radio or X-ray core flux densities.

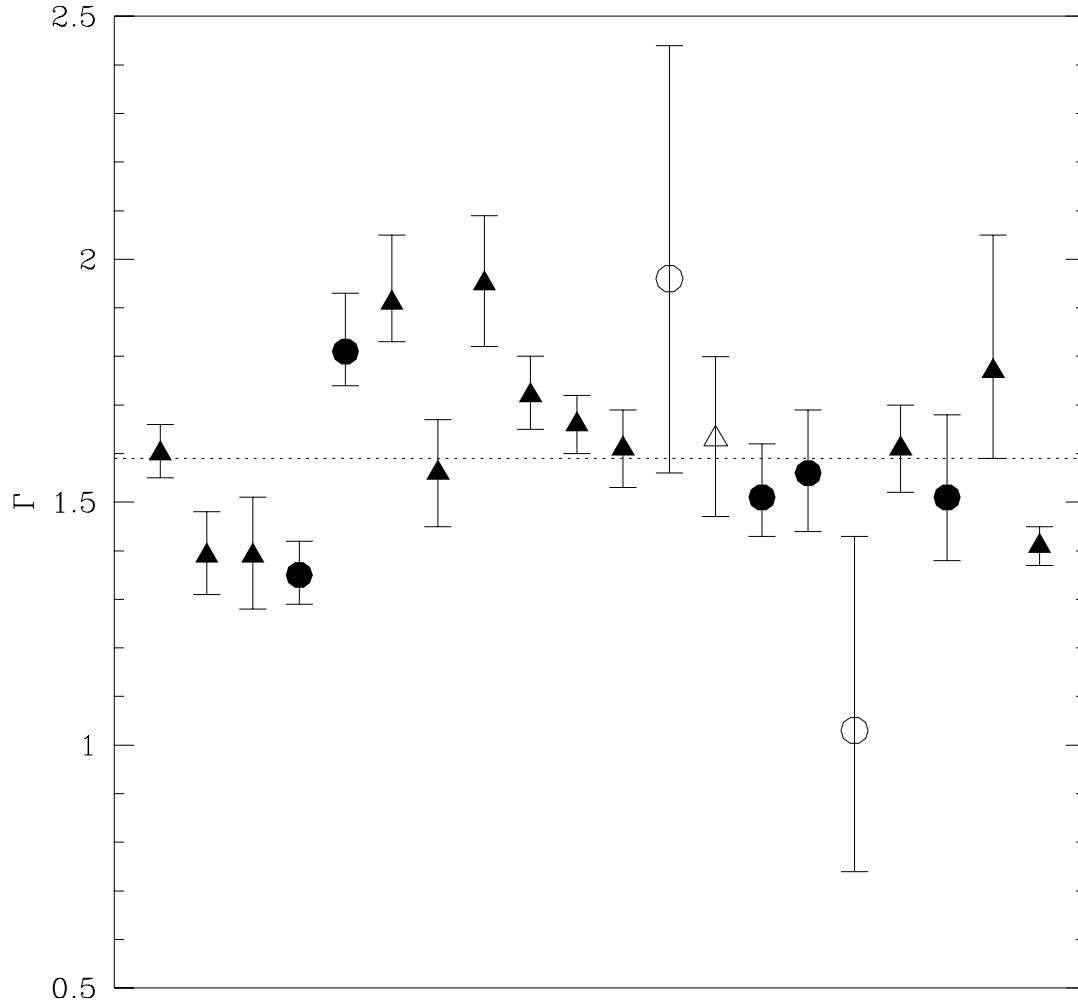


FIG. 5.— X-ray spectral indices of the cores. Objects are in RA order, as in Table 4. Objects with X-ray jet emission are shown as triangles, and those without as circles. Unfilled symbols mark the three low-redshift objects of our sample. The dotted horizontal line is the best-fit photon index (given by  $\Gamma = \alpha_x + 1$ ).

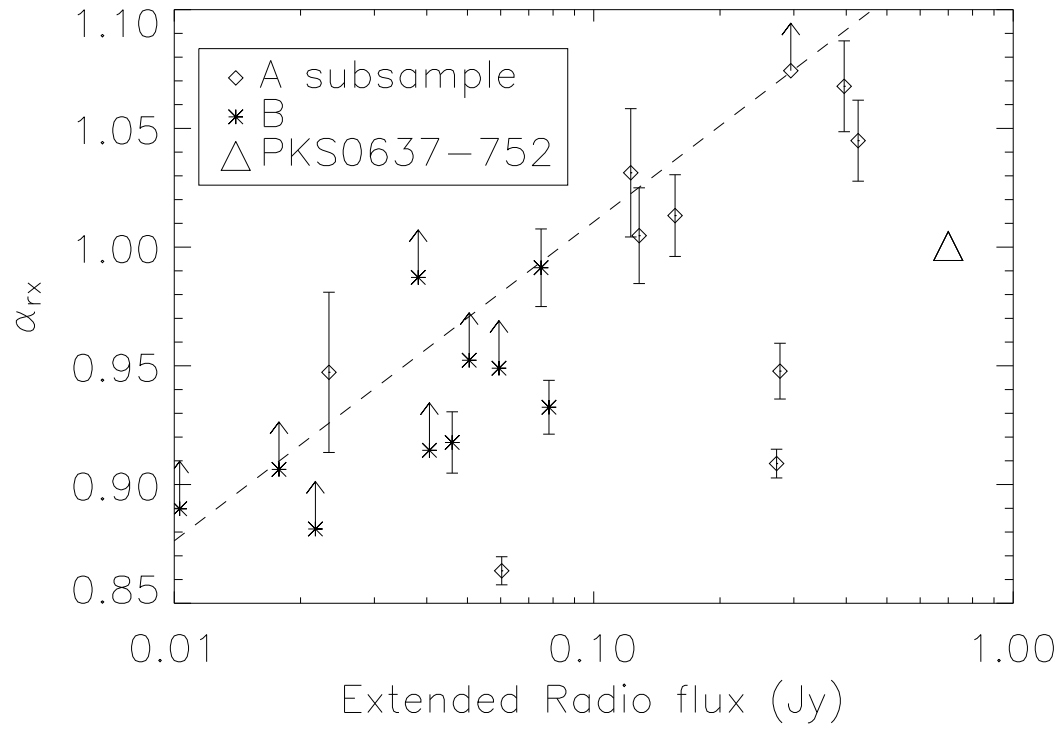


FIG. 6.— Plot of  $\alpha_{rx}$  against radio flux density in the extended emission. The result for PKS 0637–752 is given for comparison. The dashed line gives the limit to  $\alpha_{rx}$  for a hypothetical observation where the limit to the X-ray count rate is 0.003 count/s. Actual limits vary from source to source due to the varying angular sizes and locations of the radio jets. Sources included in our survey that satisfy only the subsample B category (based on morphology) are more likely to be X-ray faint, which reduces the limiting value of  $\alpha_{rx}$ .

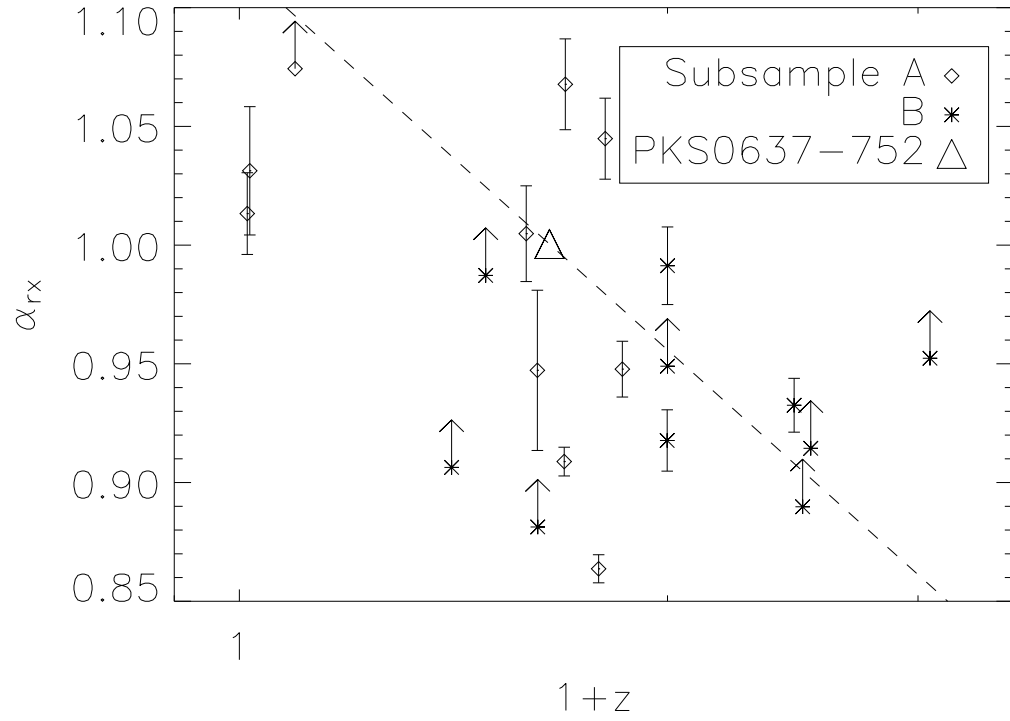


FIG. 7.— Plot of  $\alpha_{rx}$  against redshift. The result for PKS 0637–752 is given for comparison. The dashed line gives the dependence of  $\alpha_{rx}$  on  $z$  under the assumptions that the X-ray emission results only from inverse Compton scattering off of the cosmic microwave background and that the beaming parameters for all jets are the same as those of PKS 0637–752, so that the X-ray flux density would increase as  $(1+z)^4$ . Clearly, there is a wide distribution of the observed values of  $\alpha_{rx}$ , indicating that the beaming parameters vary widely. We set  $z = 1$  for the source without a measured redshift.

TABLE 1  
QUASARS IN THE COMPLETE SAMPLE

B1950	Name	$z^a$	$m_V$	$S_5$		Subsample	
				Core (Jy)	Jet <sup>b</sup> (mJy)	(A)	(B)
0106+013	4C +01.02	2.099	18.5	3.841	198	A	B
0144-522	PKS	-	17.5	0.189	47	-	B
0208-512	PKS	0.999	17	3.053	127	-	B
0229+131	4C +13.14	2.059	17.5	1.118	100	-	B
0234+285	4C +28.04	1.213	19	2.464	50	-	B
0256+075	PKS	0.893	18.5	0.552	18	-	B
0402-362	PKS	1.417	17	1.838	19	-	B
0413-210	PKS	0.808	19	1.027	342	A	B
0454-463	PKS	0.858	18	1.088	289	A	-
0508-220	PKS	0.1715	18.5	0.107	249	A	-
0707+476		1.292	18	0.973	44	-	B
0745+241		0.410	19	0.719	92	-	B
0748+126		0.889	18	1.43	13	-	B
0820+225	4C +22.21	0.951	19.5	1.606	283	A	B
0833+585		2.101	18	0.678	14	-	B
0858-771	PKS	0.490	17.5	0.192	117	-	B
0859+470	4C +47.29	1.462	19	1.645	149	A	B
0903-573	PKS	0.695	18.5	0.746	563	A	B
0920-397	PKS	0.591	18.5	1.29	303	A	-
0923+392	4C +39.25	0.6948	18	2.681	308	A	-
0953+254		0.712	17	0.483	9	-	B
0954+556	4C +55.17	0.909	17.5	2.568	179	A	B
1030-357	PKS	1.455	19	0.27	121	-	B
1040+123	3C 245	1.029	17	1.627	554	A	-
1046-409	PKS	0.620	18	0.494	404	A	B
1055+018	4C +01.28	0.888	18.5	2.642	76	-	B
1055+201	4C +20.24	1.110	17	0.768	858	A	B
1116+128	4C +12.39	2.118	19	1.888	122	A	B
1116-462	PKS	0.713	17	1.234	289	A	B
1145-676	PKS	-	18	1.238	137	-	B
1202-262	PKS	0.789	19.5	0.593	334	A	B
1251-713	PKS	-	21	1.432	75	-	B
1258-321	ESO 443-G024; MCG -5-31-12	0.01704	13	0.141	287	A	-
1303-827	PKS	-	17.5	0.221	260	A	-
1343-601	PKS, Cen B	0.01292	11	2.34	585	A	B
1354+195	4C +19.44	0.720	16	1.309	402	A	B
1421-490	PKS	-	24	5.261	277	A	B
1424-418	PKS	1.522	18	2.138	113	-	B
1502+106		1.839	18.5	2.198	11	-	B
1622-297	PKS	0.815	19.5	2.041	42	-	B
1641+399	3C 345; 4C +39.48	0.5928	16	8.5	475	A	B
1642+690	4C +69.21	0.751	19	0.999	155	A	B
1655+077		0.621	20.5	1.165	99	-	B
1655-776	PKS	0.0944	17.5	0.425	563	A	-
1823+568	4C +56.27	0.664	19	0.858	212	A	B
1828+487	3C 380; 4C +48.46	0.692	17	4.5	3657	A	-
1928+738	IES, 4C +73.18	0.3021	16.5	2.939	114	A	B
2007+777		0.342	16.5	0.823	14	-	B
2052-474	PKS	1.489	18.5	1.103	58	-	B
2101-490	PKS	(1.04)	17	0.524	184	-	B
2123-463	PKS	1.67	18.5	0.546	75	-	B
2201+315	4C +31.63	0.295	15.5	1.4	180	A	B
2230+114	4C +11.69	1.037	17.5	6.468	134	A	B
2251+158	3C 454.3; 4C +15.76	0.859	16	12.19	355	A	B
2255-282	PKS	0.926	17	1.602	67	-	B
2326-477	PKS	1.299	17	1.679	52	-	B

<sup>a</sup>Redshifts were obtained from the NASA Extragalactic Database except for 2101-490, which is taken from Gelbord & Marshall (2004).

<sup>b</sup>For the jets,  $S_5$  is the computed radio flux density of the extended emission based on the ATCA and VLA images and converted to 5 GHz.

TABLE 2  
OBSERVATION LOG

Target	<i>Chandra</i> Obs ID	Live Time (s)	Date (UT)
0208–512	3108	5014	2001-12-13
0229+131	3109	5410	2002-01-30
0413–210	3110	4862	2002-04-08
0745+241	3111	5019	2002-03-07
0858–771	3112	4962	2002-06-19
0903–573	3113	4934	2002-07-04
0920–397	3114	4466	2002-07-04
1030–357	3115	5539	2002-05-07
1046–409	3116	4330	2002-04-24
1145–676	3117	4621	2002-04-24
1202–262	3118	5074	2002-03-02
1258–321	3119	5426	2002-03-08
1343–601	3120	5160	2002-07-24
1424–418	3121	4475	2002-07-04
1655+077	3122	4825	2002-04-28
1655–776	3123	4917	2002-05-21
1828+487	3124	5329	2002-05-20
2052–474	3125	5310	2002-07-29
2101–490	3126	5370	2002-08-02
2251+158	3127	4929	2002-11-06

TABLE 3  
RADIO CONTOURS

Target	Instrument	Date (UT)	Freq. (GHz)	5 × RMS noise (mJy/beam)
0208–512	<i>ATCA</i>	2002-02-01	8.64	1.275
0229+131	<i>VLA</i>	2000-11-05	1.425	1.065
0413–210	<i>VLA</i>	2000-11-05	4.86	2.540
0745+241	<i>VLA</i>	2001-05-06	4.86	0.695
0858–771	<i>ATCA</i>	2000-05-20	8.64	0.495
0903–573	<i>ATCA</i>	2002-02-04	8.64	1.345
0920–397	<i>ATCA</i>	2000-09-01	8.64	2.300
1030–357	<i>ATCA</i>	2000-05-22	8.64	0.390
1030–357 <sup>a</sup>	<i>ATCA</i>	2000-05-22	4.80	0.645
1046–409	<i>ATCA</i>	2002-05-22	8.64	0.820
1145–676	<i>ATCA</i>	2002-02-02	8.64	0.670
1202–262	<i>ATCA</i>	2000-05-22	8.64	0.500
1258–321	<i>ATCA</i>	2002-02-02	8.64	0.605
1343–601 <sup>b</sup>	<i>ATCA</i>	2002-02-02	8.64	2.155
1424–418	<i>ATCA</i>	2002-02-04	8.64	1.250
1655+077	<i>VLA</i>	2001-05-06	1.46	0.835
1655–776	<i>ATCA</i>	2002-02-05	8.64	0.830
1828+487	<i>VLA</i>	2000-11-05	4.86	1.079
2052–474	<i>ATCA</i>	2002-02-05	8.64	0.825
2101–490	<i>ATCA</i>	2000-05-25	8.64	0.610
2251+158	<i>VLA</i>	2001-05-06	4.86	8.100

<sup>a</sup>For 1030–357 (Fig. 1h), 4.8 GHz radio contours at 5 × and 10 × the RMS level are overlaid in red to show large-scale structure.

<sup>b</sup>Fig. 1m includes an extra contour at 1.293 mJy/beam (3 × the RMS level).

TABLE 4  
QUASAR X-RAY CORE MEASUREMENTS

B1950	Count Rate (cps)	Streak Rate (cps)	$N_{\text{HGal}}^{\text{a}}$ ( $10^{21} \text{ cm}^{-2}$ )	$\Gamma_{\text{x}}$	$N_{\text{Hint}}^{\text{b}}$ ( $10^{22} \text{ cm}^{-2}$ )	$S_{\text{x}}^{\text{b}}$ (nJy)	$\chi^2/(\text{dof})$
0208–512	$0.305 \pm 0.008$	$0.54 \pm 0.15$	0.294	$1.60^{+0.06}_{-0.05}$	< 0.34	$256^{+15}_{-8}$	56.2/41
0229+131	$0.111 \pm 0.005$	$0.08 \pm 0.10$	0.83	$1.39^{+0.09}_{-0.08}$	< 2.13	$102 \pm 7$	16.7/16
0413–210	$0.063 \pm 0.004$	$0.09 \pm 0.11$	0.239	$1.39^{+0.12}_{-0.11}$	< 0.69	$54^{+5}_{-4}$	4.1/7
0745+241	$0.160 \pm 0.006$	$0.23 \pm 0.16$	0.516	$1.35^{+0.07}_{-0.06}$	< 0.19	$131^{+7}_{-6}$	23.5/22
0858–771	$0.130 \pm 0.005$	$0.52 \pm 0.21$	1.021	$1.81^{+0.12}_{-0.07}$	< 0.37	$145^{+15}_{-7}$	18.1/17
0903–573	$0.123 \pm 0.005$	$0.00 \pm 0.08$	3.212	$1.91^{+0.14}_{-0.08}$	< 0.74	$199^{+26}_{-10}$	14.9/16
0920–397	$0.105 \pm 0.005$	$0.11 \pm 0.12$	2.147	$1.56 \pm 0.11$	< 0.48	$124^{+10}_{-9}$	23.3/12
1030–357	$0.069 \pm 0.004$	$0.14 \pm 0.14$	0.609	$1.95^{+0.14}_{-0.13}$	< 1.48	$78^{+7}_{-5}$	6.0/8
1046–409	$0.196 \pm 0.007$	$-0.01 \pm 0.09$	0.829	$1.72^{+0.08}_{-0.07}$	< 0.25	$202^{+11}_{-9}$	16.4/23
1145–676 <sup>c</sup>	$0.292 \pm 0.008$	$0.49 \pm 0.23$	3.189	$1.66 \pm 0.06$	< 0.08	$382^{+17}_{-16}$	69.2/38
1202–262 <sup>d</sup>	$0.147 \pm 0.005$	$0.16 \pm 0.13$	0.708	$1.61 \pm 0.08$	< 0.45	$140^{+10}_{-8}$	21.8/20
1258–321 <sup>e</sup>	$0.011 \pm 0.002$	$0.09 \pm 0.16$	0.575	$1.96^{+0.48}_{-0.40}$	< 1.76	$14^{+6}_{-3}$	6.5/2
1343–601 <sup>e</sup>	$0.252 \pm 0.007$	$0.53 \pm 0.27$	10.6	$1.63^{+0.17}_{-0.16}$	$1.08 \pm 0.24$	$870^{+240}_{-180}$	35.1/35
1424–418	$0.189 \pm 0.007$	$0.08 \pm 0.12$	0.805	$1.51^{+0.11}_{-0.08}$	< 1.37	$181^{+20}_{-11}$	13.8/23
1655+077	$0.165 \pm 0.006$	$0.09 \pm 0.14$	0.626	$1.56^{+0.13}_{-0.12}$	< 0.55	$153^{+21}_{-16}$	38.3/22
1655–776 <sup>e</sup>	$0.031 \pm 0.003$	$0.02 \pm 0.11$	0.830	$1.03^{+0.40}_{-0.29}$	< 3.17	$41^{+23}_{-9}$	4.2/2
1828+487 <sup>f</sup>	$0.421 \pm 0.009$	$0.73 \pm 0.25$	0.66	$1.61 \pm 0.09$	< 0.09	$344 \pm 10$	74.6/61
2052–474	$0.113 \pm 0.005$	$0.48 \pm 0.21$	0.404	$1.51^{+0.17}_{-0.13}$	< 1.96	$109^{+18}_{-10}$	10.3/15
2101–490	$0.060 \pm 0.003$	$0.07 \pm 0.11$	0.341	$1.77^{+0.28}_{-0.18}$	< 0.28	$65^{+17}_{-9}$	1.2/7
2251+158 <sup>g</sup>	$0.656 \pm 0.012$	$2.89 \pm 0.50$	0.713	$1.41 \pm 0.04$	< 0.12	$379 \pm 11$	80.5/89

NOTE. — Results correspond to the energy band 0.5–7 keV. Upper limits are  $3\sigma$  confidence. Otherwise uncertainties are  $1\sigma$  for one interesting parameter. Data have been grouped to a minimum of 30 counts per bin before fitting, except for 1258–321 for which statistics are poor, and the grouping is a minimum of 15 counts per bin.

<sup>a</sup>From the COLDEN program provided by the CXC, using data from Dickey & Lockman (1990), except for 0229+131 (from Murphy et al. 1996) and 1828+487 and 2251+158 (from Elvis et al. 1989)

<sup>b</sup> $S_{\text{x}}$  is the flux density at 1 keV from spectral fits. One may roughly estimate  $S_{\text{x}}$  by scaling the count rate by 1000 nJy/(count/s).

<sup>c</sup>Indication of a soft excess, not modelled here.

<sup>d</sup>The inclusion of a narrow  $\text{K}\alpha$  fluorescence line from neutral Fe at a (fixed) rest energy of 6.4 keV improves the fit significantly (5% probability of the improvement in  $\chi^2$  being by chance, on an F-test). The equivalent width is  $221^{+15}_{-109}$  eV.

<sup>e</sup>Low-redshift object not included in statistical analysis of the spectral results.

<sup>f</sup>Spectrum shows signs of pileup. Quoted results for  $\chi^2$  and the power-law slope are with the pile-up model in XSPEC applied. Without it the fit is unacceptable:  $\chi^2 = 84$ ,  $\Gamma = 1.39 \pm 0.04$ .

<sup>g</sup>Spectrum shows signs of pileup. Quoted results for  $\chi^2$  and the power-law slope are with the pile-up model in XSPEC applied. Without it the fit is unacceptable:  $\chi^2 = 116$ ,  $\Gamma = 0.79 \pm 0.03$ .

TABLE 5  
QUASAR JET MEASUREMENTS

Target	PA ( $^{\circ}$ )	$\theta_i$ ( $''$ )	$\theta_o$ ( $''$ )	$S_r^a$ (mJy)	$\nu_r$ (GHz)	Count Rate (cps)	$S_x^a$ (nJy)	$\alpha_{rx}$	$P_{jet}^b$	X? <sup>c</sup>
0208–512	-130	1.5	6.0	46.0 ± 1.0	8.64	0.0068 ± 0.0015	6.8	0.92 ± 0.01	1.33e-14	Y
0229+131	20	1.5	6.0	50.5 ± 0.7	1.42	-0.0004 ± 0.0004	< 0.7	> 0.95	9.50e-01	N
0413–210	155	1.0	4.0	426.9 ± 1.2	4.86	0.0039 ± 0.0012	3.9	1.04 ± 0.02	2.85e-08	Y
0745+241	-45	1.5	8.0	17.8 ± 0.8	4.86	0.0008 ± 0.0007	< 2.9	> 0.88	5.11e-02	N
0858–771	165	1.5	7.0	38.2 ± 0.6	8.64	0.0000 ± 0.0006	< 1.7	> 0.99	5.67e-01	N
0903–573	35	1.0	5.0	395.4 ± 0.8	8.64	0.0045 ± 0.0015	4.5	1.07 ± 0.02	1.19e-06	Y
0920–397	180	1.5	12.0	128.3 ± 2.3	8.64	0.0043 ± 0.0015	4.3	1.00 ± 0.02	3.37e-06	Y
1030–357	-150	1.5	16.0	78.2 ± 2.1	8.64	0.0089 ± 0.0017	8.9	0.93 ± 0.01	< 1e-10	Y
1046–409	130	1.5	6.0	23.4 ± 0.8	8.64	0.0021 ± 0.0012	2.1	0.95 ± 0.03	5.32e-03	Y
1145–676	70	2.0	40.0	59.4 ± 1.8	8.64	0.0015 ± 0.0012	< 5.1	> 0.95	3.74e-02	N
1202–262	-15	1.5	8.0	60.3 ± 0.9	8.64	0.0225 ± 0.0022	22.5	0.86 ± 0.01	< 1e-10	Y
1258–321	-70	1.5	20.0	122.5 ± 1.7	8.64	0.0026 ± 0.0012	2.6	1.03 ± 0.03	6.35e-04	Y
1343–601	-120	1.5	11.0	156.3 ± 2.5	8.64	0.0045 ± 0.0013	4.5	1.01 ± 0.02	2.46e-08	Y
1424–418	-110	1.0	4.0	40.6 ± 0.7	8.64	0.0018 ± 0.0015	< 6.3	> 0.91	4.85e-02	N
1655+077	-50	1.5	5.0	21.7 ± 0.6	4.86	-0.0006 ± 0.0007	< 1.4	> 0.93	9.18e-01	N
1655–776	75	1.5	15.0	295.0 ± 3.6	8.64	0.0006 ± 0.0008	< 3.0	> 1.07	1.53e-01	N
1828+487	-40	1.0	2.5	272.8 ± 3.6	4.86	0.0278 ± 0.0030	27.8	0.91 ± 0.01	< 1e-10	Y
2052–474	-25	1.5	4.0	10.3 ± 0.5	8.64	0.0004 ± 0.0007	< 2.5	> 0.89	2.38e-01	N
2101–490	100	1.5	16.0	74.9 ± 1.4	8.64	0.0031 ± 0.0009	3.1	0.99 ± 0.02	< 1e-10	Y
2251+158	-50	1.5	7.0	278.0 ± 5.6	4.86	0.0142 ± 0.0029	14.2	0.95 ± 0.01	< 1e-10	Y

<sup>a</sup>The jet radio flux density is computed at  $\nu_r$  for the same region as for the X-ray count rate, given by the PA,  $r_i$ , and  $r_o$  parameters. The X-ray flux density is given at 1 keV assuming a conversion of 1  $\mu$ Jy/(count/s), which is good to  $\sim 10\%$  for power law spectra with low column densities and spectral indices ( $\alpha_x$ ) near 1.5.

<sup>b</sup>The quantity  $P_{jet}$  is defined as the chance that there are more counts than observed in the specified region under the null hypothesis that the counts are background events.

<sup>c</sup>The jet is defined to be detected if  $P_{jet} < 0.0025$  (see text).

TABLE 6  
QUASAR JET BEAMING MODEL PARAMETERS

Target	$\alpha_{rx}$	$R_1^a$ ( $10^{-3}$ )	$V^b$ ( $pc^3$ )	$B_1^c$ ( $\mu$ G)	$K^d$	$\theta^e$ ( $^{\circ}$ )	$\nu_s^f$ (MHz)
0208–512	0.92	132.8	4.2e+15	7.4	2.34	20	10.0
0229+131	> 0.95	< 55.8	7.8e+17	1.9	< 0.15	> 40	26.1
0413–210	1.04	13.0	7.0e+14	17.7	1.89	21	32.6
0745+241	> 0.88	< 230.3	2.9e+13	11.1	< 9.88	> 13	5.0
0858–771	> 0.99	< 40.3	6.4e+13	14.1	< 4.25	> 17	14.1
0903–573	1.07	10.1	3.6e+14	21.5	2.28	20	34.9
0920–397	1.00	29.8	3.6e+14	13.9	3.09	18	17.9
1030–357	0.93	103.0	1.9e+17	3.8	0.67	28	14.5
1046–409	0.95	80.0	2.0e+14	10.4	3.84	17	10.5
1145–676	> 0.95	< 77.7	3.6e+16	4.3	< 1.01	> 25	13.5
1202–262	0.86	335.5	1.3e+15	9.5	6.32	15	5.3
1258–321	1.03	18.9	4.2e+08	75.6	33.47	9	14.0
1343–601	1.01	25.8	9.1e+07	106.9	56.70	7	11.7
1424–418	> 0.91	< 140.6	5.4e+16	4.7	< 0.92	> 25	12.6
1655+077	> 0.93	< 94.7	1.6e+14	9.6	< 3.87	> 17	9.6
1655–776	> 1.07	< 9.1	9.5e+10	56.6	< 14.25	> 12	22.9
1828+487	0.91	145.3	1.3e+14	22.5	10.55	13	7.9
2052–474	> 0.89	< 214.4	3.8e+16	3.4	< 0.88	> 26	9.8
2101–490	0.99	37.6	1.4e+16	6.1	0.95	25	20.3
2251+158	0.95	72.9	1.9e+15	12.3	3.23	18	12.9

<sup>a</sup> $R_1$  is the ratio of the inverse Compton to synchrotron luminosities, given by eq. 2.

<sup>b</sup> $V$  is the volume of the synchrotron emission region.

<sup>c</sup> $B_1$  is the minimum energy magnetic field, given by eq. 1.

<sup>d</sup> $K$  is a function of observable and assumed quantities given by eq. 3.

<sup>e</sup>The bulk Lorentz factor is assumed to be 10. This assumption would not be appropriate for 1343–601 because the extended material is not likely to be relativistic.

<sup>f</sup>The frequency  $m\nu_s$  gives the part of the synchrotron spectrum radiated by electrons that up-scatter CMB photons to 1 keV.